

Self-Regenerative Ni-Doped CaTiO₃/CaO for Integrated CO₂ Capture and Dry Reforming of Methane

Seongbin Jo and Kandis Leslie Gilliard-AbdulAziz*

In this work, a new type of multifunctional materials (MFMs) called self-regenerative Ni-doped CaTiO₃/CaO is introduced for the integrated CO₂ capture and dry reforming of methane (ICCDRM). These materials consist of a catalytically active Ni-doped CaTiO₃ and a CO₂ sorbent, CaO. The article proposes a concept where the Ni catalyst can be regenerated in situ, which is crucial for ICCDRM. Exsolved Ni nanoparticles are evenly distributed on the surface of CaTiO₃ under H₂ or CH₄, and are re-dispersed back into the CaTiO₃ lattice under CO₂. The Ni-doped CaTiO₃/CaO MFMs show stable CO₂ capture capacity and syngas productivity for 30 cycles of ICCDRM. The presence of CaTiO₃ between CaO grains prevents CaO/CaCO₃ thermal sintering during carbonation and decarbonation. Moreover, the strong interaction of CaTiO₃ with exsolved Ni mitigates severe accumulation of coke deposition. This concept can be useful for developing MFMs with improved properties that can advance integrated carbon capture and conversion.

1. Introduction

Integrated CO_2 capture and utilization (ICCU) has been widely studied as a promising climate mitigation strategy for producing CO_2 -derived fuels or chemicals such as methane, synthetic gas (syngas, CO, and H_2), light olefins, and methanol. [1] ICCU is a less energy-intensive process compared to conventional CO_2 capture and utilization (CCU). Conventional CCU involves separating CO_2 from waste streams through carbonation (capture) and decarbonation (regeneration), transporting it via pipelines, and converting it into value-added chemicals. [2] ICCU uses dual functional materials (DFMs), catalysts combined with CO_2 sorbents, to directly convert captured CO_2 into fuels and chemicals without separating and transporting CO_2 . [3] Ni/CaO-based dual functional materials (DFMs) are commonly used in ICCU processes due to the excellent catalytic activity

o. Jo

Mork Family Department of Chemical Engineering and Materials Science University of Southern California

Los Angeles, California 90089, USA K. L. Gilliard-AbdulAziz

Sonny Astani Department of Civil and Environmental Engineering University of Southern California

Los Angeles, California 90089, USA E-mail: kabdulaz@usc.edu

The ORCID identification number(s) for the author(s) of this article can be found under https://doi.org/10.1002/smll.202401156

DOI: 10.1002/smll.202401156

of Ni and theoretical CO2 capture capacity of CaO (17.8 mmol CO2/g CaO) at temperatures ranging from 500 to 700 °C, which are relevant for CO₂ valorization. [3,4] For example, Ni/CaO-based DFMs have been applied to various ICCU schemes such as methanation, [3,4c] reverse water gas shift (rWGS),[4c,d] dry reforming of methane (DRM),[4b,c,e,f] and oxidative dehydrogenation of ethane to ethylene.[5] Among the reactions studied, the Integrated CO₂ capture and subsequent DRM (ICCDRM) process using Ni/CaO-based DFMs is a promising strategy to convert two greenhouse gases, CO₂ and CH₄, into useful industrial building blocks - syngas.[4b,c,e,f]

The initial step for ICCDRM occurs when CO_2 is chemically absorbed from a waste stream by CaO to form $CaCO_3$ in the carbonation step, $CaO(s) + CO_2(g) \leftrightarrow$

CaCO₃(s). Then the desorbed CO₂ from CaCO₃ reacts with CH₄ to produce syngas via DRM over the adjacent Ni catalyst, CaCO₃(s) + CH₄(g) \leftrightarrow CaO(s) + 2CO(g) + 2H₂(g). [4b.c] ICCDRM exhibits excellent decarbonation kinetics, CaCO₃(s) \leftrightarrow CaO(s) + CO₂(g), by shifting the equilibrium toward the products (Le Chatelier's principle) because of continuous consumption of CO₂ by DRM; CO₂(g) + CH₄(g) = 2CO(g) + 2H₂(g). [4e] However, IC-CDRM does not have sufficient multicycle performance for industrial practicality due to a sharp decrease in syngas production after complete CO₂ desorption and coke deposition from CH₄ decomposition: CH₄(g) \leftrightarrow C(s) + 2H₂(g). [4b]

Coke deposition is one of the primary deactivation mechanisms for Ni catalysts used for DRM and ICCDRM. The coke can be deposited easily over large Ni nanoparticles (>20 nm) with inherently weak interaction with the underlying support. [6] Some of the deposited coke can be gasified via the reverse Boudouard reaction, $C(s) + CO_2(g) = 2CO(g)$; however, the remaining coke can result in a gradual decrease in the CO2 capture capacity and catalyst performance. [4a-c,e] The coke deposition can form metal carbides that decompose into carbon and metal atoms or clusters.[7] Continuous carbon accumulation can cause filamentous or whisker coke to separate active Ni metal nanoparticles from the support. [7b] Filamentous coke is difficult to oxidize or remove because the interface between the metal nanoparticles and support is thermodynamically-stable.[8] Therefore, enhancing the interaction between Ni and oxide supports/sorbents is essential to maintain catalytic performance and stability.

Another factor that diminishes the multicycle performance of Ni/CaO-based materials for ICCDRM is the low thermal stability of CaO. The stress induced by the cyclical volume expansion and

www.small-journal.com

1613889, 2024, 36, Downloaded from https://onlinelibrary.wiley.com/doi/1.01002/sml1202401156 by University Of Southern California, Wiley Online Library on [05/02/2025]. See the Terms and Conditions, wiley.com/remers-and-conditions) on Wiley Online Library frontes of use; OA articles are governed by the applicable Creative Commons

shrinkage from CaO to CaCO₃ (CaO: 16.9 cm³ g⁻¹ and CaCO₃: 36.9 cm³ g⁻¹) during carbonation and decarbonation^[9] can contribute to rapid pore collapse of the structure. Additionally, the lower Tammann temperature of CaCO₃ (533 °C) than the DRM operation temperature (≈700 °C) causes the loss of surface area and sintering-induced decrease in CO₂ capture capacity.^[9,10] During each cycle, the reversible phase transformation of CaO to CaCO₃ weakens the Ni-CaO metal support interaction, resulting in significant sintering of Ni nanoparticles.[11]

The use of in-situ exsolved metal nanoparticles from a select family of reducible perovskite oxides (ABO₃) has been utilized to address issues such as coking and sintering in DRM reaction conditions.[12] The perovskite oxide structure (ABO₃) consists of a large A-site cation (La, Nd, Ca, Sr, or Ba) and a smaller B-site cation (Ti, Fe, Co, or Ni) where catalytic metals are substituted.[12f,13] There are many benefits to using exsolution to generate catalyst nanoparticles. For instance, the nanoparticles formed are homogeneously distributed throughout the support.^[14] The inherent strong interaction between the partially submerged (or socketed) exsolved metal nanoparticles and host perovskites can retard the thermal sintering of metal nanoparticles.[15] The exsolved metal nanoparticles can undergo self-regeneration by re-incorporating into the host perovskite under oxidative conditions and then re-exsolving under reductive conditions. The self-regeneration mechanism can also suppress coke accumulation during redox experiments by in situ gasification to CO_x by surface lattice oxygen of the perovskite oxide. [12b,16] The partially submerged or socked nanoparticles can also suppress filamentous coke growth between the metal nanoparticles and perovskite support.[17]

The morphology of CaO plays an essential role in the CO₂ capture kinetics, CO₂ uptake capacity, and thermal stability.^[9,18] To improve the sinter-resistance behavior of CaO, inert metal oxide stabilizers with high Tammann temperatures, such as ZrO₂, SiO₂, Al₂O₃, CeO₂ or MgO, are introduced into the CaO structure. The CaO/CaCO3 stabilization with oxide additives can improve CO₂ capture performance (kinetics and capacity) by enhancing CO₂ diffusion within the porous structure and preventing the densification of the CaO particles.[9] In addition, inert oxide materials between CaO crystallite grains can minimize CaCO₃ volume expansion during the CO₂ capture step, alleviating the stress-induced sintering of CaO.[9]

To make ICCDRM commercially viable, addressing issues such as enhancing CO2 uptake capacity, sintering of CaO and Ni, and coke deposition is vital. This study discusses an exciting approach to improve ICCDRM multicycle stability by developing self-regenerative Ni/CaTiO₃/CaO multifunctional materials (MFMs). The Ni nanoparticles are exsolved from Ca(Ni, Ti_{1,x})O₃ perovskite oxide. The strong adherence of exsolved Ni nanoparticles to Ca(Ni_xTi_{1,x})O₃ perovskite decreases the Ni sintering rate and coke formation, allowing for long-term multicycle catalytic stability. The strong metal-support interaction between Ni and CaTiO₃ suppresses the growth of filamentous coke. Coke formed on the surface of Ni nanoparticles during the DRM step is gasified by CO2 during carbonation. The Ni nanoparticles are also self-regenerated during the CO₂ capture step (oxidative conditions) and re-emerged during the subsequent DRM (reductive conditions). The presence of CaTiO₃ perovskite phase within CaO grains alleviates the thermal sintering of CaO/CaCO₃ phases.

The Ni/CaTiO₃/CaO MFMs were characterized for their CO₂ capture capacity and ICCDRM performance. The experiments were developed to elucidate the property function relation for Ni/CaTiO₃/CaO MFMs.

2. Results and Discussion

2.1. Structural, Morphological, and Textural Properties of Ni-Doped CaTiO₃/CaO MFMs

Figure 1a illustrates the schematic of Ni incorporation into the CaTiO₃ perovskite frameworks during calcination and in-situ Ni exsolution from Ca_{1+x}Ni_vTi_{1-v}O₃ perovskite during the ICCDRM process. For this study, $Ca_{1+x}Ni_vTi_{1-v}O_3$ perovskite materials with secondary phase of CaO were calcined at 800 °C to incorporate Ni into CaTiO₃ and avoid the formation of perovskite-like structures containing higher Ca/Ti ratios, such as Ca₃Ti₂O₇ and Ca₄Ti₃O₁₀, which form at higher temperatures above 1000 °C [19] and are nonreducible materials. The emergence of Ni occurs under a reductive environment (i.e., H2) at 800 °C. During the CO2 capture step, the Ni nanoparticles are re-incorporated into the perovskite Ca_{1+x}Ni_vTi_{1-v}O₃ matrix and CaO capture CO₂ as a formation of CaCO₃. Then the Ni nanoparticles are exsolved (e.g., selfregeneration of Ni nanoparticles), CO2 desorbed from CaCO3 reacts with CH₄ to produce syngas (CO and H₂) during the DRM

The X-ray diffraction (XRD) patterns of Ca₁Ti₁, Ca₂Ti₁, $\text{Ca}_2\text{Ni}_{0.02}\text{Ti}_{0.98,}$ and $\text{Ca}_2\text{Ni}_{0.05}\text{Ti}_{0.95}$ were compared to investigate the crystalline structure of the synthesized MFMs (Figure 1b,c). For comparison, the XRD pattern of Ca2Ni005 DFM was also measured (Figure S1, Supporting Information). As-prepared Ca₂Ni_{0.05} DFM showed sharp peaks of CaO (JCPDS No. 75–0264) and broad NiO (JCPDS No. 73-1519) without any CaNi alloy phases. After reduction at 800 °C, NiO was converted to Ni metal (JCPDS No. 45–1027). The $Ca_2Ni_{0.02}Ti_{0.98}$ and $Ca_2Ni_{0.05}Ti_{0.95}$ MFMs were synthesized with excess Ca to promote the formation of CaO/CaTiO₂ composite materials. The concentration of Ni was changed to determine the influence on the catalytic performance and regeneration capability. Empirically, when the tolerance factor (t) lies in the range of 0.8 - 1.0, the structure of perovskites is stable.[20] Although the tolerance factor is a good predictor of the perovskite stability, the octahedron factor (μ), a constant used to predict lattice distortion, must lie in the range of 0.44 - 0.72 for B and O to form a stable BO₆ octahedron. The tolerance factor (t) and octahedron factor (μ) of CaTiO₃ are 0.97 and 0.45, respectively, indicating that a stable CaTiO₃ perovskite structure is expected. On the other hand, the tolerance factor (t) and the octahedron factor (µ) of CaNiO₃ are 1.01 and 0.39, respectively, meaning that NiO₆ octahedron would be unstable to form CaNiO₃ perovskite structures. The XRD patterns of Ca₁Ti₁ exhibited sharp peaks of orthorhombic CaTiO₃ perovskite phase (ICPDS No. 86-1393) without impurity. The prominent peaks located at 33.1, 47.5, and 59.4 2theta correspond to the (1 1 2), (2 2 0), and (2 0 4) lattice planes of the CaTiO₃ structure. The XRD patterns of Ca₁Ti₁, Ca₁Ni_{0.01}Ti_{0.99}, and Ca₁Ni_{0.02}Ti_{0.98} showed the sharp peaks of CaTiO₃ perovskite phase without a separate CaO phase (Figure S2a, Supporting Information). Although a small amount of Ni is added, the patterns of NiO peak was observed in MFMs with a Ca-to-(Ni+Ti) ratio

16136829, 2024, 36, Downloaded from https://onlinelibrary.wiley.com/doi/10.1002/smll.2024011.56 by University Of Southern California, Wiley Online Library on [05/02/2025]. See the Terms

ns) on Wiley Online Library for rules of use; OA articles are governed by the applicable Creative Commons

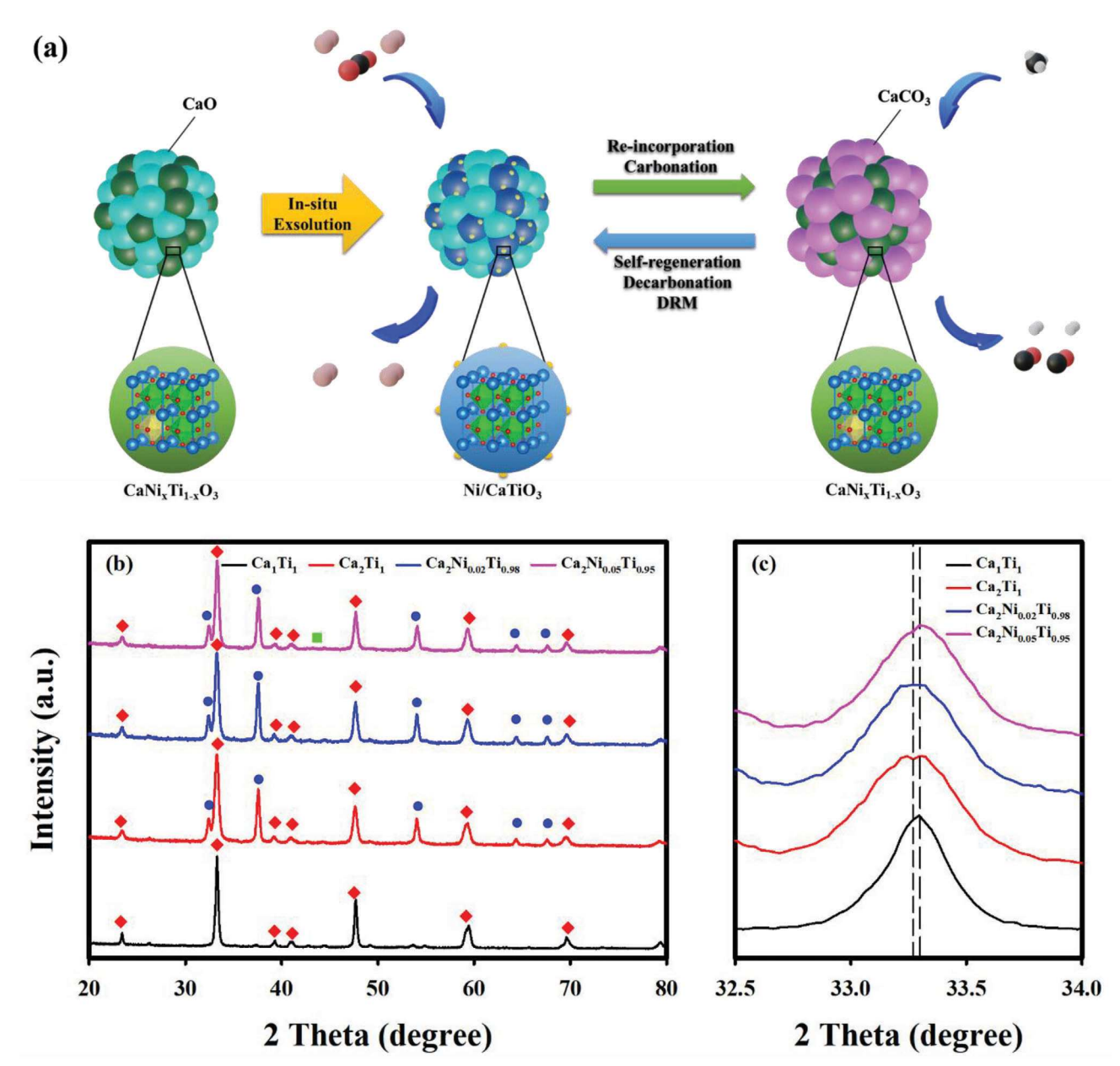


Figure 1. a) Schematic of in situ Ni nanoparticle exsolution from $Ca_{1+x}Ni_yTi_{1-y}O_3$ perovskite and Ni re-incorporation into $CaTiO_3$ perovskite during ICCDRM process, b) XRD patterns and c) enlarged local XRD pattern of Ca_1Ti_1 , Ca_2Ti_1 , $Ca_2Ni_{0.02}Ti_{0.98}$ and $Ca_2Ni_{0.95}Ti_{0.95}$: \spadesuit CaTiO₃, \blacksquare , \blacksquare NiO.

of 1, such as $Ca_1Ni_{0.01}Ti_{0.99}$ and $Ca_2Ni_{0.02}Ti_{0.98}$ (Figure S2b and Table S1, Supporting Information), which corresponds to the estimation from the predicted tolerance and octahedron factor for $CaNiO_3$. For Ca_2Ti_1 , $Ca_2Ni_{0.02}Ti_{0.98}$, and $Ca_2Ni_{0.05}Ti_{0.95}$, it was observed that $CaTiO_3$ perovskite and CaO formed instead of the $Ca_3Ti_2O_7$ and $Ca_4Ti_3O_{10}$ phase. For $Ca_2Ni_{0.05}Ti_{0.95}$ MFM, a small NiO peak was observed. However, the peak of NiO was not observed in the $Ca_2Ni_{0.02}Ti_{0.98}$ MFM, showing a maximum solubility capacity for Ni dopants in the $CaTiO_3$ lattice (Figure S3a, Supporting Information). Estimated Ca/(Ni+Ti) ratio in perovskite obtained from STEM-EDS of as-prepared $Ca_1Ni_{0.01}Ti_{0.99}$, $Ca_2Ni_{0.02}Ti_{0.98}$, and $Ca_2Ni_{0.05}Ti_{0.95}$ are 1.01, 1.01 and 1.09, respectively (Table S1, Supporting Information). All samples showed

Ca/(Ni+Ti) higher than 1, excess Ca and Ni exists as CaO and NiO, respectively. All Ni species were incorporated into CaTiO $_3$ perovskite frameworks in Ca $_2$ Ni $_{0.02}$ Ti $_{0.98}$ MFM as a formation of Ca $_{1+x}$ Ni $_y$ Ti $_{1-y}$ O $_3$ /(1-x)CaO without NiO separation. After reduction at 800 °C, a very small peak of Ni metal was observed in both Ca $_2$ Ni $_{0.02}$ Ti $_{0.98}$ and Ca $_2$ Ni $_{0.05}$ Ti $_{0.95}$ MFMs (Figure S3b, Supporting Information). Therefore, excess calcium promotes the formation of Ca $_{1+x}$ Ni $_y$ Ti $_{1-y}$ O $_3$ perovskite with CaO despite the unstable NiO $_6$ octahedron.

Figure 1c shows XRD patterns between 32.5 to 34° 2theta. The peak of $CaTiO_3$ perovskite shifts to lower angles from 33.3° (Ca_1Ti_1) to 33.27° (Ca_2Ti), indicating volume expansion as the ratio of Ca/Ti increases. According to the Rietveld refinement in

16136829, 2024, 36, Downloaded from https://onlinelibrary.wiley.com/doi/10.1002/smll.202401156 by University Of Southern California, Wiley Online Library on [05/02/2025]. See the Terms and Conditions (https://onlinelibrary.wiley.com/term

and-conditions) on Wiley Online Library for rules of use; OA articles are governed by the applicable Creative Commons

www.small-journal.com

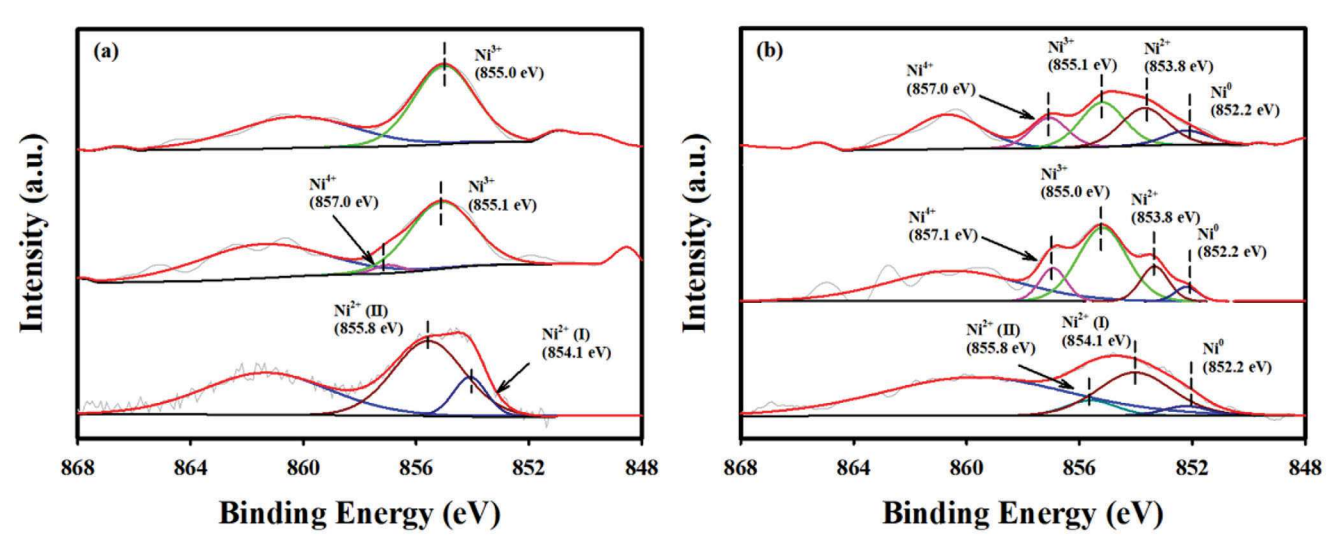


Figure 2. Ni 2p_{3/2} XPS spectra of a) as prepared and b) reduced Ca₂Ni_{0.05}, Ca₂Ni_{0.05}Ti_{0.98} and Ca₂Ni_{0.05}Ti_{0.95}.

Table 1, the lattice parameters of a, b, and c of CaTiO₃ for Ca₁Ti₁ are 5.443, 7.648, and 5.389 Å, respectively. The lattice parameters of a, b, and c for Ca₂Ti₁ are 5.457, 7.658, and 5.402, respectively, which are slightly larger than those of Ca₁Ti₁, leading to volume expansion from 224.32 to 225.76 Å³. Conversely, the diffraction peaks corresponding to CaTiO₃ shifted to a higher angle as the Ni/Ti ratio increased, implying lattice shrinkage owing to the substitution of Ti with Ni.^[21] It was also observed that the lattice parameters of a, b, and c of Ca₂Ni_{0.02}Ti_{0.98} and Ca₂Ni_{0.05}Ti_{0.95} MFMs are smaller than those of Ca₂Ti, and the lattice volume decreased.

X-ray photoelectron spectroscopy (XPS) analysis was conducted for as-prepared and reduced $Ca_2Ni_{0.05}$, $Ca_2Ni_{0.02}Ti_{0.98}$ and $Ca_2Ni_{0.05}Ti_{0.95}$. The C-C component peak at 284.8 eV was used to calibrate the XPS raw data (Figure S4, Supporting Information). In the C 1s XPS spectra of all samples, adventitious C-C peak at 284.8 eV and CO_3^{2-} peak at \approx 289 eV were observed. [22] In the sample containing CaO, strong basic site, XPS spectra of CO_3^{2-} peak was high, which might be the CO_2 adsorption in the XPS chamber. In the Ni $2p_{3/2}$ XPS spectrum of $Ca_2Ni_{0.05}$ DFM, an asymmetric doublet peak of NiO was revealed by the Gaussian-Lorentzian curve fitting, with the peaks located at 8541.1 and 855.8 eV, and a broad satellite peak at higher binding energy at \approx 861 eV (**Figure 2**). [23] The peak centered at 854.1 eV is attributed to the surface bulk NiO, $Ni^{2+}(I)$, whereas the peak at 855.6 eV

Table 1. Refined cell parameters of Ca $_1$ Ti $_1$, Ca $_2$ Ti $_1$, Ca $_2$ Ni $_{0.02}$ Ti $_{0.98}$, and Ca $_2$ Ni $_{0.05}$ Ti $_{0.95}$ from XRD patterns.

	Quantity (%) CaTiO ₃ /CaO	Lattice parameters (Å)			Lattice volume (Å)
		а	Ь	С	
Ca ₁ Ti ₁	100/-	5.442	7.655	5.387	224.078
Ca ₂ Ti ₁	74/26	5.457	7.658	5.402	225.761
$Ca_2Ni_{0.02}Ti_{0.98}$	70/30	5.446	7.647	5.395	224.655
Ca ₂ Ni _{0.05} Ti _{0.95}	69/31	5.445	7.650	5.399	224.881

is related to the NiO interacting with CaO, Ni²⁺(II). [^{4e,24}] In literatures, the Ni²⁺(I)/Ni²⁺(II) ratio decreased with an increase in Ca-to-Ni molar ratio in Ni/CaO DFMs. [^{4e]} For Ca₂Ni_{0.02}Ti_{0.98} and Ca₂Ni_{0.05}Ti_{0.95} MFMs, two different peaks at 857.2 eV and 855.1 eV are attributed to Ni⁴⁺ and Ni³⁺ species, respectively, whereas bulk NiO, Ni²⁺(I), peak was not observed. [^{25]} Although Ni 2p spectra were unclear because of low Ni amount in the samples, metallic Ni peak at 852.2 eV was observed in all samples after reduction. The Ni⁴⁺ and Ni³⁺ peaks decreased and Ni²⁺ (853.6 eV) and Ni⁰ (852.4 eV) peaks appeared. The existence of Ni⁴⁺ and Ni³⁺ species implies that not all Ni species were exsolved from the host Ca_{1+x}Ni_yTi_{1-y}O₃ perovskite. The detection of Ni²⁺ species implies that Ni⁰ on the surface might be oxidized before measuring XPS results in the chamber. [^{23b}]

In the Ca 2p XPS spectra of CaO and Ca $_2$ Ni $_{0.05}$ DFM, Ca $2p_{3/2}$ (350.4 eV) and Ca $2p_{1/2}$ (346.9 eV) doublet were observed with a separation of 3.5 eV and intensity ratio of 1/2,^[26] and binding energy values remained constant after reduction (**Figure 3**). For Ca $_2$ Ni $_{0.02}$ Ti $_{0.98}$ and Ca $_2$ Ni $_{0.05}$ Ti $_{0.95}$ MFMs, Ca 2p spectra was deconvoluted into two CaO peaks (350.4 and 346.9 eV) and two CaTiO $_3$ peaks (349.4 and 345.9 eV).^[27] After reduction, an increase in the ratio of CaO to CaTiO $_3$ was observed, resulting from the Ni and CaO exsolution from the host Ca $_{1+x}$ Ni $_y$ Ti $_{1-y}$ O $_3$ perovskite.

For Ti 2p XPS spectrum of CaTiO₃, two main distinct peaks were observed at 463.9 and 458.2 eV (**Figure 4**). [27] It is clearly seen that the Ti 2p XPS spectra of $\text{Ca}_2\text{Ni}_{0.02}\text{Ti}_{0.98}$ and $\text{Ca}_2\text{Ni}_{0.05}\text{Ti}_{0.95}$ MFMs shifted to lower binding energy after Ni incorporation, and the spectra further shifted with increasing Ni-to-Ti ratio. After reduction, the binding energy values of the MFMs are comparable to that of bare CaTiO₃ perovskite, implying Ni exsolution from the $\text{Ca}_{1+x}\text{Ni}_v\text{Ti}_{1-v}\text{O}_3$.

The XPS spectra for O 1s profiles is broad and complicated due to the overlapping peaks of oxygen in lattice of NiO, CaO and CaTiO₃, oxygen defect (oxygen vacancies) and adsorbed oxygen (**Figure 5**). The O 1s XPS spectrum of CaO contained main peaks located at 531.3 with minor at 532.5 eV, corresponding to lattice oxygen of CaO and adsorbed water or surface hydroxyls

16136829, 2024, 36, Downloaded from https://onlinelibrary.wiley.com/doi/10.1002/smll.202401156 by University Of Southern California, Wiley Online Library on [05/02/2025]. See the Terms and Conditions (https://online

ns) on Wiley Online Library for rules of use; OA articles are governed by the applicable Creative Commons

www.small-journal.com

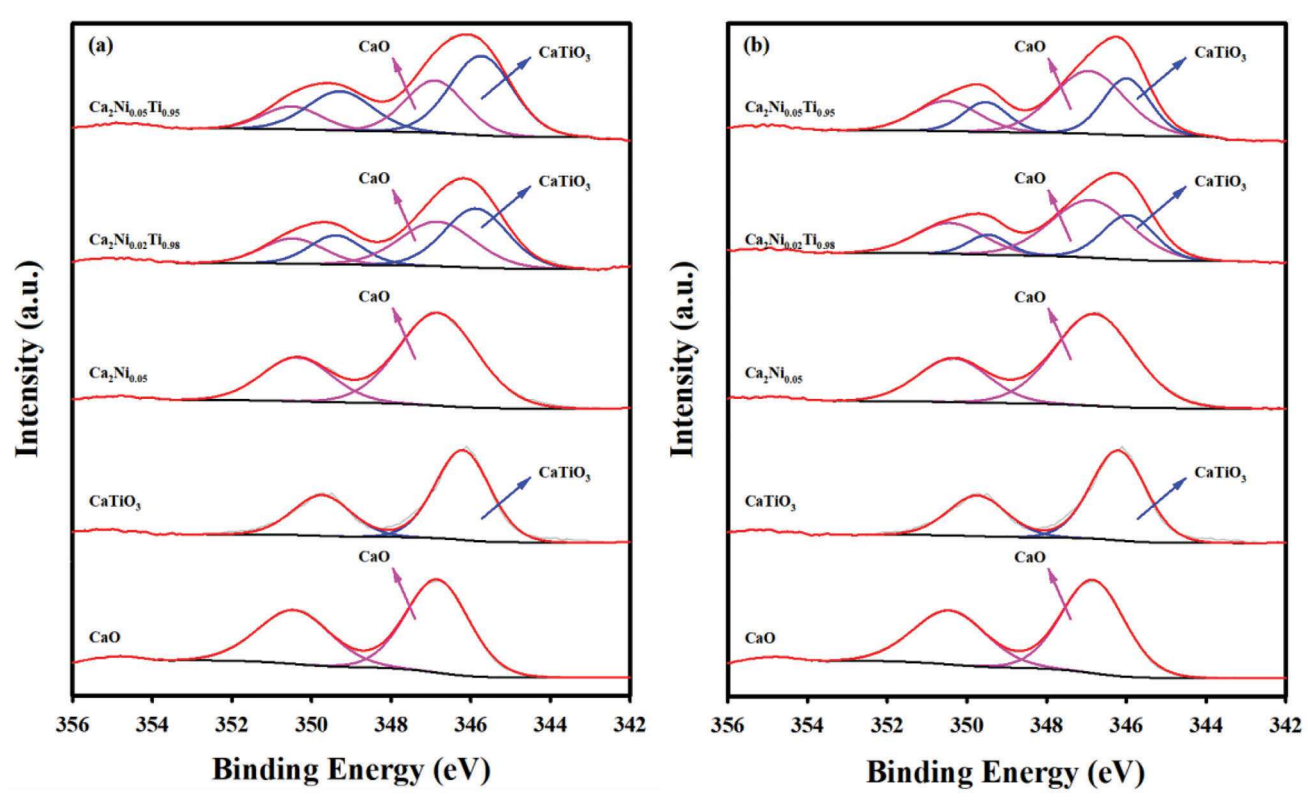
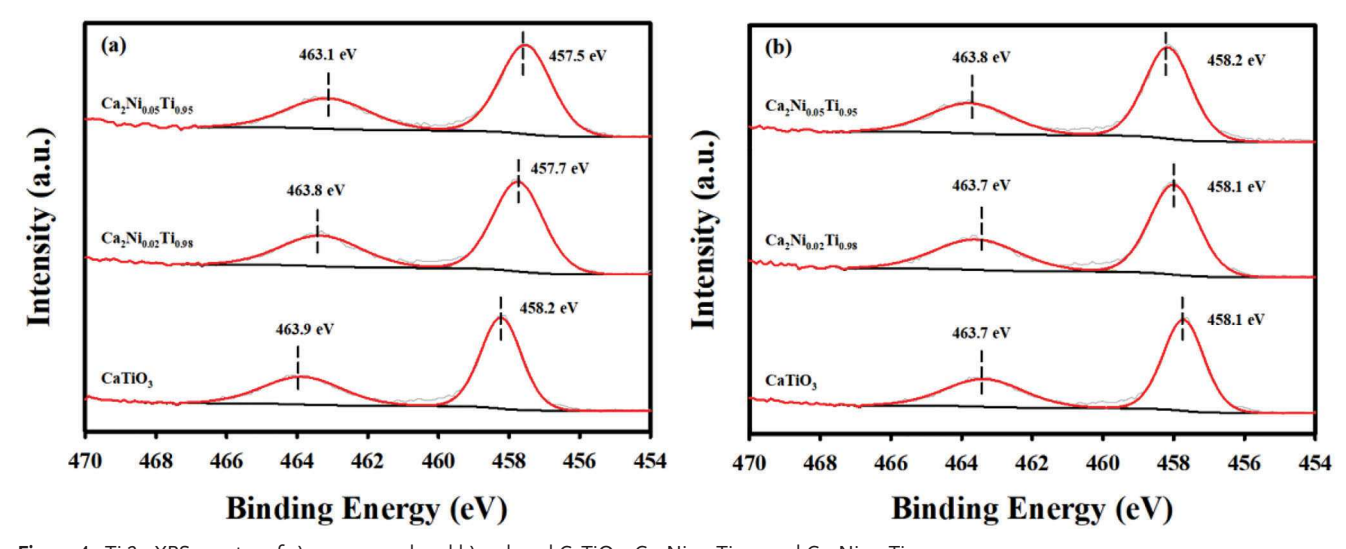


Figure 3. Ca 2p XPS spectra of a) as prepared and b) reduced CaO, CaTiO₃, Ca₂Ni_{0.05}, Ca₂Ni_{0.02}Ti_{0.98} and Ca₂Ni_{0.05}Ti_{0.95}.

on CaO. [28] In the O 1s XPS spectrum of CaTiO $_3$, two peaks were deconvoluted at 531.3 and 529.3 eV, which are attributed to adsorbed oxygen in CaTiO $_3$ and lattice oxygen, respectively. [27] For Ca $_2$ Ni $_{0.05}$ DFM, two peaks for lattice oxygen of NiO and CaO overlapped at \approx 531.5 eV, and the peak intensity decreased slightly after reduction, which might be reduction of NiO. Compared to CaTiO $_3$, a higher peak at \approx 531.2 eV was observed in Ca $_2$ Ni $_{0.02}$ Ti $_{0.98}$ and Ca $_2$ Ni $_{0.05}$ Ti $_{0.95}$ MFMs, because of CaO exis-

tence. The binding energy of two peaks decreased with increasing Ni ratio. The binding energy values increased after reduction, which are comparable to the spectra of CaO and CaTiO3. In addition, the ratio of peak ($\approx 531.4~\rm eV$)-to-peak ($529.1~\rm eV$) decreased in the Ca2Ni_0.05 Ti_0.95 MFM after reduction, which might be reduction of NiO on the surface. Based on the XRD and XPS results, it is clearly observed that the incorporated Ni species can be exsolved from the Ca1+xNi_vTi_1,vO3 perovskite.

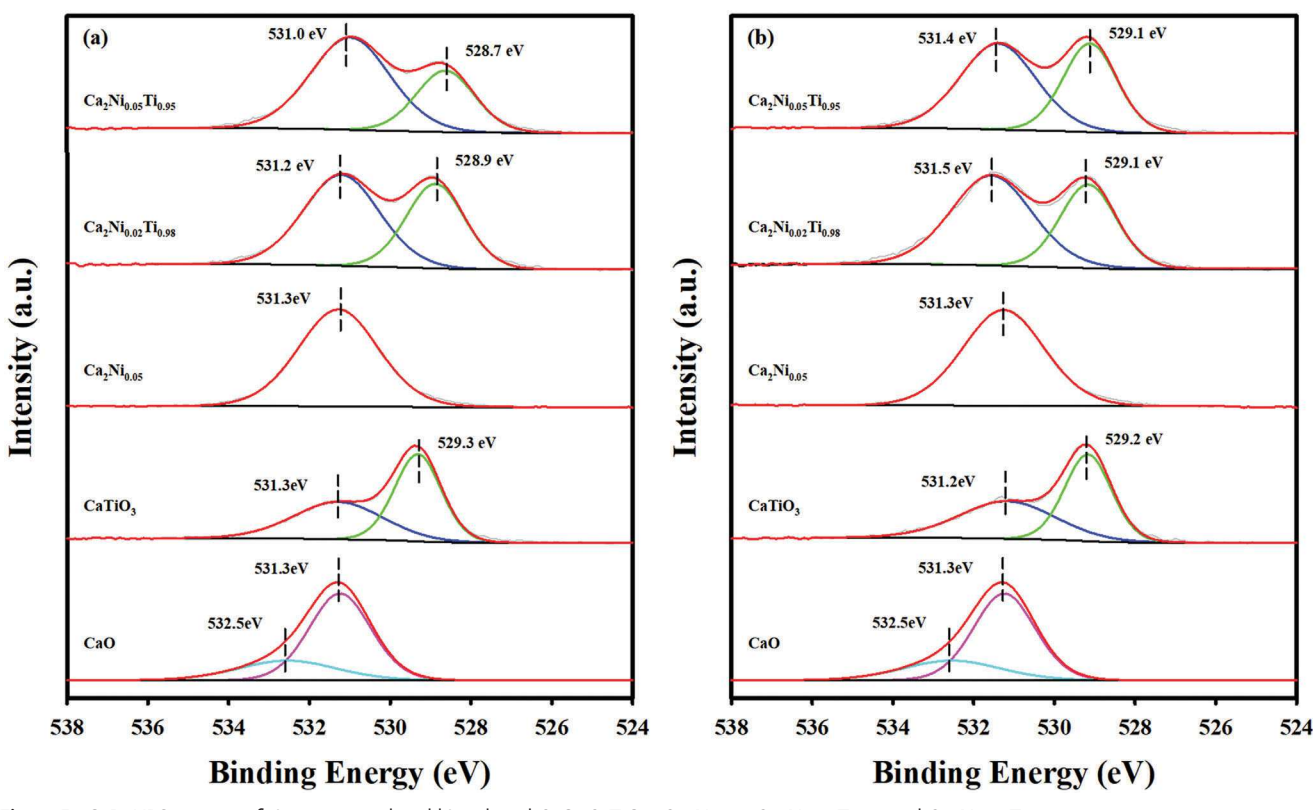


 $\textbf{Figure 4.} \ \ \text{Ti 2p XPS spectra of a) as prepared and b) reduced } \ \ \text{Ca}_{2} \text{Ni}_{0.02} \text{Ti}_{0.98} \ \ \text{and } \ \ \text{Ca}_{2} \text{Ni}_{0.05} \text{Ti}_{0.95}.$

16136829, 2024, 36, Downloaded from https://onlinelibrary.wiley.com/doi/10.1002/smll.202401156 by University Of Southern California,

, Wiley Online Library on [05/02/2025]. See the Terms and Conditions (https://onlinelibrary.wiley

and-conditions) on Wiley Online Library for rules of use; OA articles are governed by the applicable Creative Commons



 $\textbf{Figure 5.} \hspace{0.2cm} \textbf{O} \hspace{0.1cm} \textbf{1s} \hspace{0.1cm} \textbf{XPS} \hspace{0.1cm} \textbf{spectra of a)} \hspace{0.1cm} \textbf{as} \hspace{0.1cm} \textbf{prepared and b)} \hspace{0.1cm} \textbf{reduced CaO, CaTiO}_3, \hspace{0.1cm} \textbf{Ca}_2 \textbf{Ni}_{0.05}, \hspace{0.1cm} \textbf{Ca}_2 \textbf{Ni}_{0.02} \textbf{Ti}_{0.98} \hspace{0.1cm} \textbf{and} \hspace{0.1cm} \textbf{Ca}_2 \textbf{Ni}_{0.05} \textbf{Ti}_{0.95}. \\ \textbf{CaPin}_{0.05} \textbf{Ti}_{0.05} \textbf{$

To investigate the self-regeneration properties of Ni (in-situ Ni exsolution from Ca_{1+x}Ni_xTi_{1-x}O₃ and Ni re-dissolving to CaTiO₃ perovskite) under the ICCDRM conditions, Scanning Transmission Electron Microscopy (STEM) High-angle annular dark field imaging (HAADF) experiments with energy-dispersive spectroscopy (EDS) were conducted. Ca₂Ni_{0.02}Ti_{0.98} MFM was selected to observe the self-regeneration of Ni nanoparticles, as no excess NiO species were present on the CaTiO3 surface in the asprepared state. The STEM EDS-mapping images of as-prepared Ca₂Ni_{0.02}Ti_{0.98} MFM, cubic/cuboid CaO, and Ca_{1+x}Ni_xTi_{1-y}O₃ perovskite are strongly coupled (Figure 6a). Ni species on the surface of the material were not observed in the as-prepared Ca₂Ni_{0.02}Ti_{0.98} MFM. STEM-EDS images of Ca₂Ni_{0.05} DFM were also measured, and NiO nanoparticles with crystallite size of \approx 25 nm were unevenly dispersed on the cubic CaO in the STEM EDS-mapping of Ca₂Ni_{0.05} DFM (Figure S5, Supporting Information). Ni nanoparticles (i.e., NiO) with an average crystallite size of \approx 25 nm were observed in Ca₂Ni_{0.05}Ti_{0.95} MFM (Figure S6, Supporting Information), corresponding to the XRD and XPS results. Although not all Ni nanoparticles are incorporated into CaTiO₃ (i.e., Ca_{1+v}Ni_vTi_{1-v}O₃), they are supported on CaTiO₃ perovskite, which might result in a stronger interaction between Ni and CaTiO3 than that between Ni and CaO.

After H2-reduction at 800 °C for 1 h, in situ exsolved Ni nanoparticles were distributed evenly on the surface of CaTiO₃ support (Figure 6b). The Ni nanoparticle size distribution was obtained from the STEM mapping of Ca2Ni002Ti098 and Ca2Ni0.05Ti0.95 MFMs (Figures S8 and S9, Supporting Information). It is observed in the STEM-HAADF images of

Ca₂Ni_{0.02}Ti_{0.98} MFMs that the Ni nanoparticles are exsolved from Ca_{1+x}Ni_xTi_{1-y}O₃ host perovskite (Figure S7, Supporting Information). For Ca2Ni_{0.05}Ti_{0.95} MFM, a minority of larger Ni nanoparticles (≈23 nm) were observed, as corroborated by XRD, which coexisted with the in-situ exsolved Ni nanoparticles. The average crystallite size of exsolved Ni nanoparticles in Ca2Ni002Ti098 and Ca₂Ni_{0.05}Ti_{0.95} were 7.06 and 7.48 nm, respectively (Figures S8 and Figure \$9, Supporting Information). In the STEM-HAADF image, it is clearly observed that the exsolved Ni nanoparticles were socketed in the host perovskite (Figures \$10 and \$11, Supporting Information). It is expected that the in-situ exsolved Ni nanoparticles formed from bulk-to-surface diffusion have a stronger interaction with CaTiO₃ and smaller crystallite size than the Ni nanoparticles deposited on the surface of CaTiO₃.

The reduced Ca₂Ni_{0.02}Ti_{0.98} MFM was re-oxidized under CO₂ capture condition (10% CO₂/He condition at 700 °C for 1 h) to investigate the morphology change of exsolved Ni nanoparticles and the composite materials. In the STEM image of Ca2Ni0.02Ti0.98 MFM after re-oxidation with CO2, the exsolved Ni nanoparticles were dispersed throughout the CaTiO3 and reincorporated into the subsurface of CaTiO₃ perovskite (Figure 6c; Figure S12, Supporting Information). Some Ni nanoparticles socketed in the CaTiO₃ perovskite still exist, however, the crystallite size of Ni nanoparticles is much smaller than the exsolved Ni nanoparticles (Figure 6b). The regeneration of larger Ni nanoparticles could have been hindered by the kinetics of re-dissolution, which is an important parameter for predicting the regeneration of exsolved nanoparticles. In addition, CO2 was chemically absorbed on the CaO grains as a formation of CaCO₃ (Figure \$13,

Wiley Online Library on [05/02/2025]. See the Terms

on Wiley Online Library for rules of use; OA articles are governed by the applicable Creative Commons

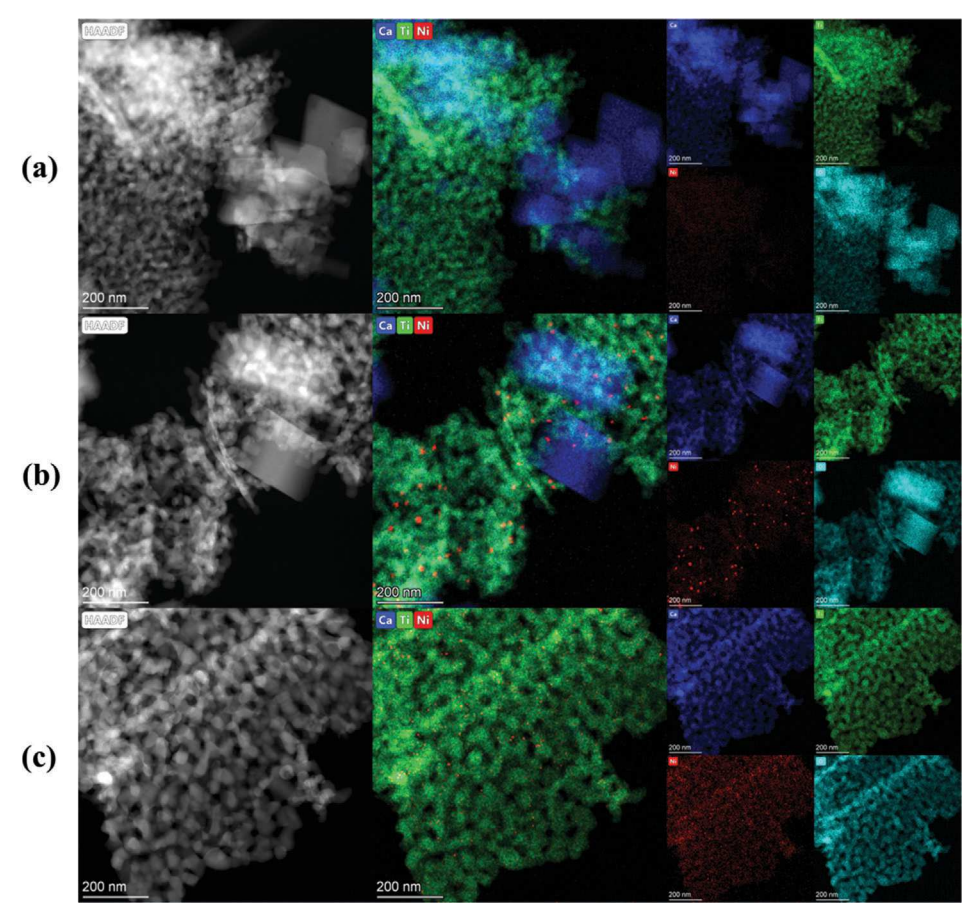


Figure 6. STEM-HAADF images of $Ca_2Ni_{0.02}Ti_{0.98}$ MFM in the states of a) as-prepared, b) reduced by H_2 at 800 °C, and c) re-oxidized by CO_2 after CO_2 capture at 700 °C.

Supporting Information). It is expected that the volume expansion of $CaCO_3$ grains by CO_2 capture would not affect Ni exsolution at the subsequent DRM step, because $CaCO_3$ grains were separated from the host $Ca_{1+x}Ni_vTi_{1-v}O_3$ perovskite.

bulk NiO (360 °C) in the $Ca_2Ni_{0.05}$ DFM, implying that NiO interaction with $CaTiO_3$ is slightly stronger than that with CaO. The second reduction peak at 495 °C is attributed to the reduction of

2.2. Enhanced Ni-CaTiO₃ Metal-Support Interaction

Figure 7 shows H₂-Temperature programmed reduction (H₂-TPR) results of Ca2Ni0.05, Ca2Ni0.02Ti0.98 and Ca2Ni0.05Ti0.95 from 100 to 800 °C with temperature ramping of 10 C min⁻¹, to investigate metal-support interaction. All samples were pretreated under 20% O₂/He at 800 °C for 1 h, to desorb adsorbed gases such as CO₂ and H₂O and to avoid lattice oxygen loss of perovskite. $\text{Ca}_2\text{Ni}_{0.05}$ shows a sharp peak centered at 430 °C with shoulder at 455 °C, which are attributed to overlapped reduction peak of bulk NiO and NiO interacting with CaO, respectively. [4e] Ca₂Ni_{0.02}Ti_{0.98} MFM shows one broad peak corresponding to Ca_{1+x}Ni_vTi_{1-v}O₃ reduction at 450 to 550 °C, which is higher than the reduction of bulk NiO. The reduction peak of bulk NiO was not observed, which is consistent with XRD result. Ca2Ni0.05 Ti0.95 MFM exhibited two overlapping peaks at 460 and 500 °C, respectively. The first reduction peak is ascribed to the reduction of NiO interacting with CaTiO₃ at 460 °C. The onset temperature of the first peak is 430 °C, which is higher than that of the reduction peak of

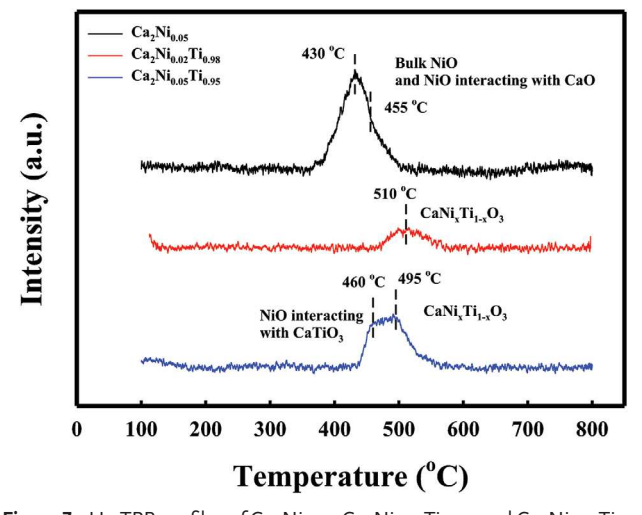


Figure 7. H_2 -TPR profiles of $Ca_2Ni_{0.05}$, $Ca_2Ni_{0.02}Ti_{0.98}$, and $Ca_2Ni_{0.05}Ti_{0.95}$ under 10 vol% H_2 from 100 to 800 °C.

16136829, 2024, 36, Downloaded from https://onlinelibrary.wiley.com/doi/10.1002/smlt.020401156 by University Of Southern California, Wiley Online Library on [05/022025]. See the Terms and Conditions (https://onlinelibrary.wiley.com/doi/10.1002/smlt.020401156 by University Of Southern California, Wiley Online Library on [05/022025]. See the Terms and Conditions (https://onlinelibrary.wiley.com/doi/10.1002/smlt.020401156 by University Of Southern California, Wiley Online Library on [05/022025]. See the Terms and Conditions (https://onlinelibrary.wiley.com/doi/10.1002/smlt.020401156 by University Of Southern California, Wiley Online Library on [05/022025]. See the Terms and Conditions (https://onlinelibrary.wiley.com/doi/10.1002/smlt.020401156 by University Of Southern California, Wiley Online Library on [05/022025]. See the Terms and Conditions (https://onlinelibrary.wiley.com/doi/10.1002/smlt.020401156 by University Of Southern California, Wiley Online Library on [05/022025]. See the Terms and Conditions (https://onlinelibrary.wiley.com/doi/10.1002/smlt.020401156 by University Of Southern California, Wiley Online Library on [05/022025]. See the Terms and Conditions (https://onlinelibrary.wiley.com/doi/10.1002/smlt.020401156 by University Of Southern California, Wiley Online Library on [05/022025]. See the Terms and Conditions (https://onlinelibrary.wiley.com/doi/10.1002/smlt.020401156 by University Of Southern California, Wiley Online Library on [05/022025]. See the Terms and Conditions (https://onlinelibrary.wiley.com/doi/10.1002/smlt.020401156 by University Of Southern California, Wiley Online Library on [05/022025]. See the Terms and Conditions (https://onlinelibrary.wiley.com/doi/10.1002/smlt.020401156 by University Of Southern California, Wiley Online Library on [05/022025]. See the Terms and Conditions (https://onlinelibrary.wiley.com/doi/10.100401156 by University Of Southern California, Wiley Online Library on [05/02025]. See the Terms and Condition (https://onlinelibrary.wiley.com/doi/10.100401156 by Un

and-conditions) on Wiley Online Library for rules of use; OA articles are governed by the applicable Creative Commons

www.small-journal.com

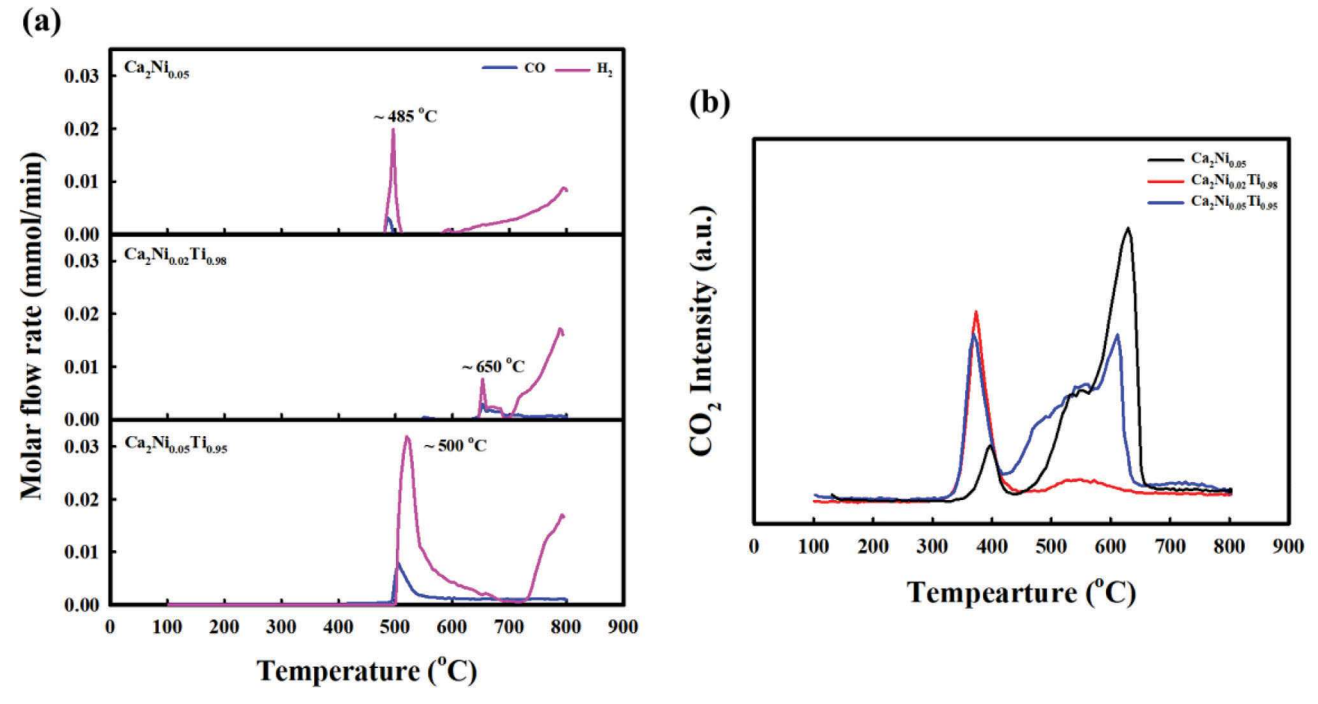


Figure 8. a) CH₄-TPR under 10 vol% CH₄ from 100 to 800 °C and b) TPO after CH₄-treatement at 800 °C for 1 h over Ca₂Ni_{0.05}, Ca₂Ni_{0.05}, Ca₂Ni_{0.05}, and Ca2Ni0.05Ti0.95.

 $Ca_{1+x}Ni_vTi_{1-v}O_3$ reduction, which is lower slightly than that in the $Ca_2Ni_{0.02}Ti_{0.98}$ MFM.

To investigate the metal support interaction between Ni nanoparticles socketed in CaTiO₃ and reaction performance over reduced Ni under CH₄ condition, CH₄-TPR tests of Ca₂Ni_{0.05}, $Ca_2Ni_{0.02}Ti_{0.98}$, and $Ca_2Ni_{0.05}Ti_{0.95}$ were conducted in the presence of 10 vol% CH4 from 100 to 800 °C with temperature ramping of 10 °C min⁻¹ (Figure 8a). All samples were pretreated under 20 vol% O₂/He at 800 °C for 1 h to desorb gases such as CO2 and H2O and to avoid oxygen loss in the CaTiO3 lattice for Ca2Ni0.02Ti0.98 and Ca2Ni0.05Ti0.95. CH4 partial oxidation (POx), MeOx(s) + CH₄(g) \leftrightarrow MeOx_{- δ}(x) + CO(g) + 2H₂(g), is accompanied by Ni species (NiO or Ca_{1+x}Ni_xTi_{1-x}O₃) reduction. In-situ exsolution of Ni nanoparticles was also observed after CH_4 -treatment at 800 °C for 1 h over the $Ca_2Ni_{0.02}Ti_{0.98}$ and Ca2Ni0.05Ti0.95 MFMs in STEM-EDS mapping (Figure S14, Supporting Information). The onset temperatures of CH₄ POx over $Ca_2Ni_{0.05}$, $Ca_2Ni_{0.02}Ti_{0.98}$, and $Ca_2Ni_{0.05}Ti_{0.95}$ are ≈ 485 , ≈ 650 , and ≈500 °C, respectively. CH₄ POx at low temperatures (485 – 550 °C) is attributed to NiO reduction for Ca₂Ni_{0.05} and $\text{Ca}_2\text{Ni}_{0.05}\text{Ti}_{0.95}\text{,}$ whereas CH₄ POx at $\approx\!\!650$ °C is ascribed to Ni species reduction in Ca_{1+x}Ni_yTi_{1-y}O₃ perovskite for Ca₂Ni_{0.02}Ti_{0.98}. For Ca₂Ni_{0.05}Ti_{0.05} MFM, onset temperature of CH₄ POx by reduction of NiO (≈500 °C) is slightly higher than that of NiO species in $Ca_2Ni_{0.05}$ DFM (485 °C), $NiO(s) + CH_4(g) \leftrightarrow Ni^0(s) +$ CO(g) + 2H₂(g), because the interaction between Ni and CaTiO₃ in Ca2Ni0.05Ti0.95 MFM is stronger than that between Ni and CaO in $Ca_2Ni_{0.05}$ DFM. In addition, the broad H_2 peaks (550 – 700 °C) are attributed to the reduction of Ca_{1+x}Ni_vTi_{1-v}O₃. For $Ca_2Ni_{0.02}Ti_{0.98}$ MFM, the reduction of $Ca_{1+x}Ni_yTi_{1-y}O_3$ between 650 and 700 °C, $Ca_{1+x}Ni_{v}Ti_{1-v}O_{3-\delta}(s) + \beta CH_{4}(g) \leftrightarrow \alpha Ni^{0} + \alpha CaO +$

 $Ca_{1+x-\alpha}Ni_{y-\alpha}Ti_{1-y}O_{3-\delta'}(s) + \beta CO(s) + 2\beta H_2(g)$, is much higher than that for Ca₂Ni_{0.05}Ti_{0.95} MFM. After H₂ reduction of Ca₂Ni_{0.02}Ti_{0.98} MFM, CH₄ POx by the reduction of Ca_{1+x}Ni_xTi_{1-x}O₃ was not observed during the CH₄-TPSR (Figure S15, Supporting Information). It is assumed that NiO on the surface of CaTiO3 in the $Ca_2Ni_{0.05}Ti_{0.95}$ MFM was reduced first by CH_4 (≈ 500 °C), and then products (CO and H₂) as reducing gases promoted Ni species reduction in the Ca_{1+x}Ni_vTi_{1-v}O₃ (550 – 700 °C). Notably, the interaction between Ni species and support materials is as follows: $Ca_2Ni_{0.02}Ti_{0.98} >> Ca_2Ni_{0.05}Ti_{0.95} > Ca_2Ni_{0.05}$.

After NiO reduction, H2 was produced over Ca2Ni0.05 DFM at temperatures higher than 600 °C, which is CH₄ decomposition over reduced Ni, $CH_4(g) \leftrightarrow C(s) + 2H_2(g)$. In contrast, for Ca₂Ni_{0.02}Ti_{0.98} and Ca₂Ni_{0.05}Ti_{0.95} MFMs, H₂ gases were produced above 700 °C, which is accompanied by CO production from in situ coke gasification by $CaTiO_3$, $CaTiO_3(s) + C(s) \leftrightarrow CaTiO_{3-\delta}(s)$ + δ CO(g). Although the Ca₂Ni_{0.05} DFM was reduced at lower temperatures, CH₄ decomposition activity at 800 °C is lower than that of Ca₂Ni_{0.02}Ti_{0.98} and Ca₂Ni_{0.05}Ti_{0.95} MFMs because of poor Ni dispersion (Table S2, Supporting Information). This phenomenon was also observed in the CH₄-TPR of the bare CaTiO₃ perovskite (Ca₁Ti₁), making CO and H₂ at temperatures higher than 600 °C (Figure \$16, Supporting Information).

Figure 8b shows the temperature programmed oxidation (TPO) profiles of $Ca_2Ni_{0.05}$, $Ca_2Ni_{0.02}Ti_{0.98}$, and $CaO_2Ni_{0.05}Ti_{0.95}$ after CH4 treatment at 800 °C for 1 h. It is widely recognized that the temperature of coke combustion is highly dependent on its location and properties. A lower combustion temperature of the deposited coke leads to increased oxygenation, while proximity to the active site catalyzes combustion. Closer proximity of coke to catalysts is usually observed in the form of encapsulating

Wiley Online Library on [05/02/2025]. See the Terms and Conditions (https://onlinelibrary.wiley

ons) on Wiley Online Library for rules of use; OA articles are governed by the applicable Creative Common

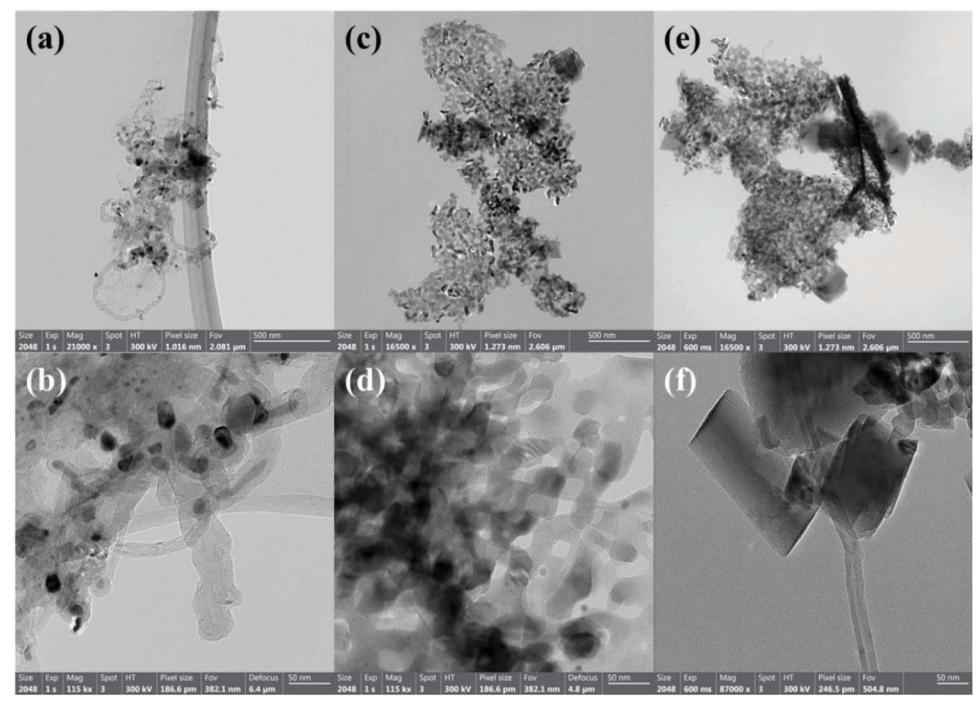


Figure 9. HRTEM images of a,b) Ca₂Ni_{0.05}, c,d) Ca₂Ni_{0.02}Ti_{0.98}, and e,f) Ca₂Ni_{0.05}Ti_{0.95} after CH₄-treatment under 10 vol% CH₄/He at 800 °C for 1 h.

coke, whereas filamentous coke is located away from the metallic sites. Three different types of CO2 peaks can be identified in the TPO profiles for $Ca_2Ni_{0.05}$, $Ca_2Ni_{0.02}Ti_{0.98}$, and $Ca_2Ni_{0.05}Ti_{0.95}$ at 300 - 400 °C (Type I), 400 - 600 °C (Type II) and 550 - 650 °C (Type III). [8] The peaks at lower temperatures (Type I) correspond to the combustion of a non-filamentous or encapsulating coke closer to the active sites catalyzing coke combustion. The peaks at higher temperatures (Type II) are ascribed to the filamentous coke between the catalysts and support materials, which have grown from the catalyst's surface. However, the Type III CO₂ peaks are assumed to be the desorption of CO2 captured by CaO at lower temperatures during the TPO because there is no O2 consumption in this range (Figure S17, Supporting Information). Ca₂Ni_{0.05} DFM shows a small amount of Type I coke combustion at ≈400 °C and a higher fraction of overlapped Type II and III CO2 peaks at temperatures between 450 and 650 °C, indicating filamentous coke deposition. Noticeable filamentous coke was observed between Ni and CaO in high-resolution transmission spectroscopy (HRTEM) in (**Figure 9a**,b). For Ca₂Ni_{0.02}Ti_{0.98} MFM, non-filamentous coke combustion (Type I) between 330 and 450 °C and small peaks of filamentous coke combustion (Type II) between 500 and 600 °C were observed. Filamentous coke is less likely to be deposited between exsolved Ni nanoparticles and CaTiO₃ due to the submerged interaction with the perovskite oxide, and filamentous coke deposition was observed in $\text{Ca}_2\text{Ni}_{0.02}\text{Ti}_{0.98}$ MFM (Figure 9c,d). Although the intensity of type I coke combustion for $Ca_2Ni_{0.02}Ti_{0.98}$ and $Ca_2Ni_{0.05}Ti_{0.95}$ MFMs are comparable, $Ca_2Ni_{0.05}Ti_{0.95}$ MFM exhibited higher CO_2 intensity of type II and III because larger Ni nanoparticles coexisted with in-situ exsolved smaller Ni nanoparticles in Ca₂Ni_{0.05}Ti_{0.95} MFM. Compared to Ca₂Ni_{0.05} DFM, the Type II coke in Ca₂Ni_{0.05}Ti_{0.95} MFM was gasified at lower temperatures, meaning closer proximity of Ni nanoparticles to coke deposited. A small amount of filamentous coke between Ni and CaTiO3 perovskite was observed (Figure 9e,f). Despite the higher CH₄ decomposition activity, smaller size of Ni nanoparticles, strong interactions between socketed Ni and host CaTiO3 perovskite, and lattice oxygen of $CaTiO_3$ in the $Ca_2Ni_{0.02}Ti_{0.98}$ MFM could alleviate the filamentous coke deposition during the ICCDRM at lower temperature (700 °C). It is also expected that the deposited coke on the surface of Ni nanoparticles (Type I) during the DRM step is likely to be gasified by CO₂ to CO during the subsequent CO₂ capture step, $C(s) + CO_2(g) \leftrightarrow 2CO(g)$.

2.3. ICCDRM Performance

CH₄-TPSR after CO₂ capture was conducted over Ca₂Ni_{0.02}Ti_{0.98} MFM to determine the optimal reaction temperature for the ICC-DRM process (Figure 10a). Prior to CH₄-TPSR, the Ca₂Ni_{0.02}Ti_{0.98} MFM was carbonated under 10 vol% CO₂/He condition at 700 °C for 1 h. The onset temperature of CO₂ desorption was observed at ≈620 °C during the TPD under pure He condition (Figure S18, Supporting Information). As expected, the reincorporated Ni species (Ca_{1+v}Ni_vTi_{1-v}O₃ phase) during the CO₂ capture step can be reduced at ≈680 °C, which is accompanied by CH_4 POx $Ca_{1+x}Ni_vTi_{1-v}O_{3-\delta}/(1-x)CaCO_3(s) + (\beta+1-x)CH_4(g) \leftrightarrow$ $\alpha \text{Ni}^{0}/\text{Ca}_{1-x} \text{Ni}_{v-\alpha} i \text{Ti}_{1-v} \acute{O}_{3-\delta'} \acute{(s)} + (\beta+1-x) \text{CO}(g) + 2(\beta+1-x) \text{H}_{2}(g)$ as mentioned above. Then, the desorbed CO2 and CH4 reacted to syngas (CO and H₂) via DRM over metallic Ni between 680 and 720 °C, $CO_2(g) + CH_4(g) \leftrightarrow 2CO(g) + 2H_2(g)$. During the DRM, the desorbed CO2 reacts with H2 produced from DRM to CO, $CO_2(g) + H_2(g) \leftrightarrow CO(g) + H_2O(g)$, leading to the decrease in H₂/CO ratio (below 1). After the complete DRM reaction, CH₄

16136829, 2024, 36, Downloaded from https://onlinelibrary.wiley.com/doi/10.1002/smll.202401156 by University Of Southern California, Wiley Online Library on [05/02/2025]. See the Terms

ns) on Wiley Online Library for rules of use; OA articles are governed by the applicable Creative Commons

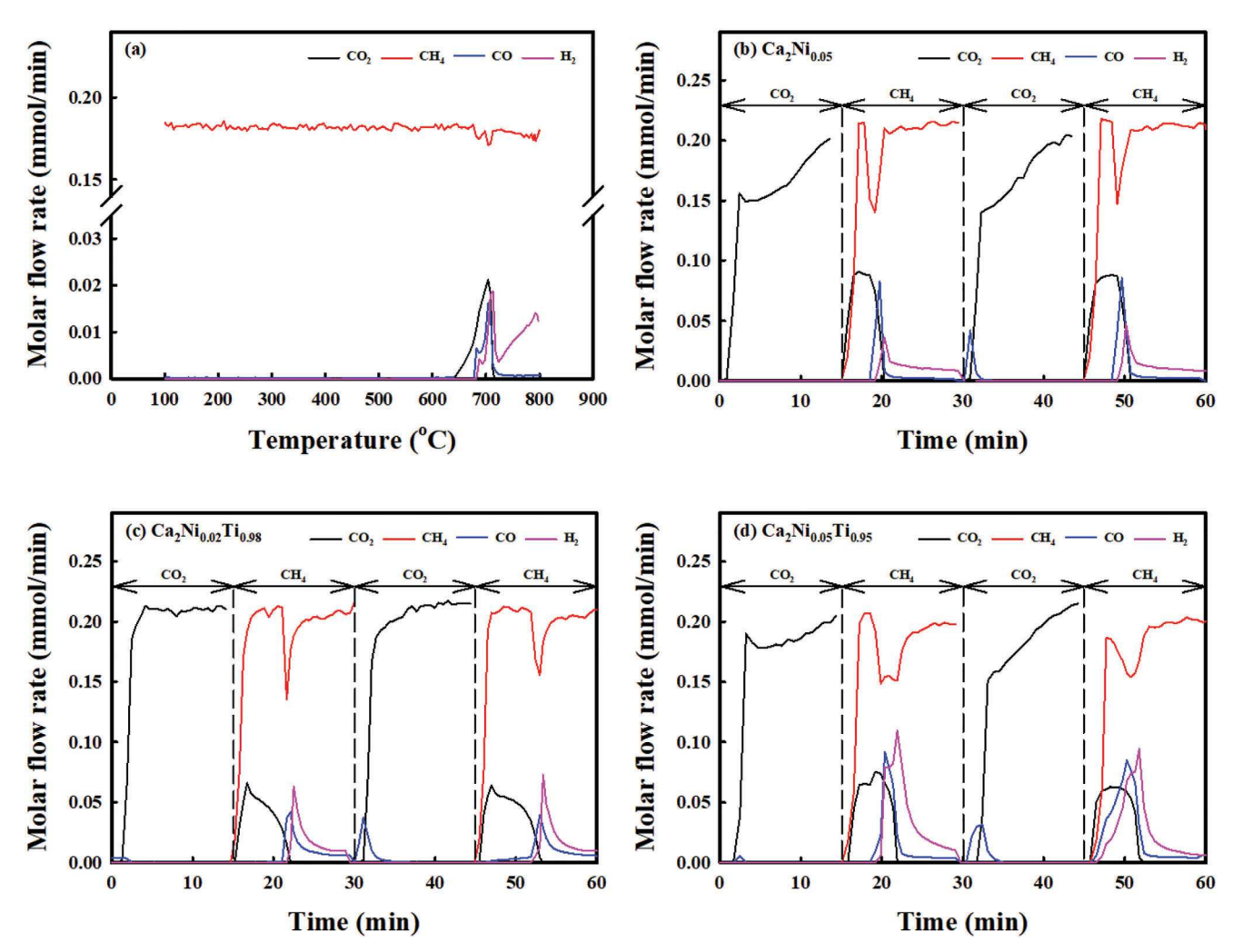


Figure 10. a) CH_4 -TPSR after CO_2 capture under 10 vol% CH_4 /He condition from 100 to 800 °C over $Ca_2Ni_{0.02}Ti_{0.98}$ MFM. CO_2 breakthrough curves and DRM profiles of b) $Ca_2Ni_{0.05}$, c) $Ca_2Ni_{0.02}Ti_{0.98}$, and d) $Ca_2Ni_{0.05}Ti_{0.95}$ in the first 2 cycles of ICCDRM at 700 °C (carbonation: 10 vol% CO_2 /He and DRM: 10 vol% CH_4 /He).

decomposed to coke and H_2 , $CH_4(g) \leftrightarrow C(s) + 2H_2(g)$, and the H₂ productivity increased with reaction temperature. During the ICCDRM over Ca₂Ni_{0.02}Ti_{0.98} MFM at 650 °C, syngas was not produced for 30 min (Figure S19, Supporting Information). The performance, such as CO2 capture and syngas production of the MFMs in the ICCDRM, was investigated during the 30 cycles of CO2 and CH4 streams at 700 °C. To study the redox properties of Ni species and consecutive reactions under CO2 and CH₄ conditions, the ICCDRM process was conducted with high WHSV (60 000 ml g h⁻¹). Figure 5b-d shows the CO₂ breakthrough curves and DRM profiles of Ca2Ni005, Ca2Ni002Ti098 and Ca₂Ni_{0.05}Ti_{0.95} in the first 2 cycles of ICCDRM and overall reactions occurred at each step (H2 reduction, CO2 capture, and DRM) in the ICCDRM are summarized in Table S3 (Supporting Information). Before the CO₂ capture step, all samples were reduced under 5 vol% H₂/He at 800 °C for 1 h, and then the temperature decreased to 700 °C under He condition. During the CO₂ capture step (10 vol% CO₂/He stream), the molar flow rate of outlet CO₂ was lower than that of inlet CO₂ at the beginning of the reaction because of CO₂ capture by CaO to form CaCO₃,

CaO(s) + CO₂(g) \leftrightarrow CaCO₃(g). In addition to the CO₂ capture by CaO, reoxidation of metallic Ni into NiO and Ca_{1+x}Ni_yTi_{1-y}O₃ was accompanied by small amount of CO production; Ni⁰(s) + CO₂(g) \leftrightarrow NiO(s) + CO(g) for Ca₂Ni_{0.05} and Ca₂Ni_{0.05}Ti_{0.95}, and α Ni⁰/Ca_{1+x-\alpha}Ni_{y-\alpha}Ti_{1-y}O_{3-\delta}(s) + β CO(g) \leftrightarrow Ca_{1+x}Ni_yTi_{1-y}O_{3-\delta}(s) + β CO(g) for Ca₂Ni_{0.02}Ti_{0.98} and Ca₂Ni_{0.05}Ti_{0.95}. XRD results also confirmed that most of the CaO in all samples was converted into CaCO₃ at 700 °C and Ni⁰ peak disappeared after carbonation (Figure S20a,b, Supporting Information).

During the subsequent DRM step (10 vol% CH_4/He stream), the CO_2 was desorbed from $CaCO_3$, and the molar flow rate of outlet CH_4 initially reached that of inlet CH_4 because of the high WHSV, as mentioned above. CH_4 reacted with the desorbed CO_2 to CO and CO_3 and CO_4 over metallic Ni, $CO_2(g) + CCO_4(g) \leftrightarrow CO_4(g) + CCO_4(g)$. The time when the highest CCO_4 conversion was achieved for CO_4 COO_4 COO_4 COO_4 and COO_4 COO_4

16136829, 2024, 36, Downloaded from https://onlinelibrary.wiley.com/doi/10.1002/smll.202401156 by University Of Southern California, Wiley Online Library on [05/02/2025]. See the Terms and Conditions (https://onlinelibrary.wiley

and-conditions) on Wiley Online Library for rules of use; OA articles are governed by the applicable Creative Commons

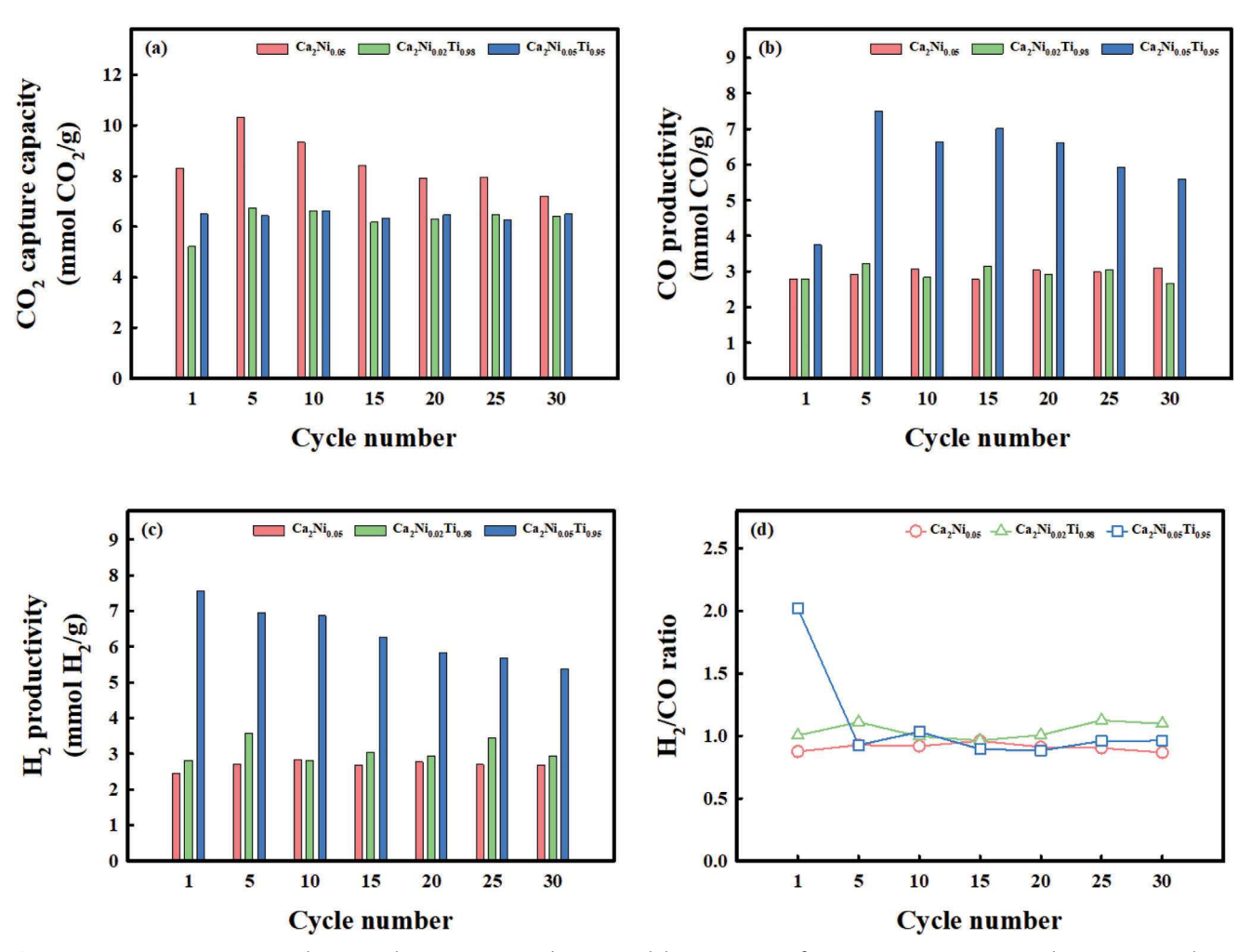


Figure 11. a) CO₂ capture capacity, b) CO productivity, c) H₂ productivity, and d) H₂/CO ratio of Ca₂Ni_{0.05}, Ca₂Ni_{0.02}Ti_{0.98}, and Ca₂Ni_{0.05}Ti_{0.95} during 30 cycles of ICCDRM at 700 °C (CO₂ capture: 10 vol% CO₂/He and DRM: 10 vol% CH₄/He).

or CaTiO₃ (Ca₂Ni_{0.05}Ti_{0.95}) were reduced fast, compared to the Ca_{1+x}Ni_vTi_{1-v}O₃ in Ca₂Ni_{0.02}Ti_{0.98}. Therefore, more desorbed CO₂ can be converted via DRM or rWGS reactions in the Ca₂Ni_{0.05} and Ca₂Ni_{0.05}Ti_{0.95}, compared to Ca₂Ni_{0.02}Ti_{0.98}. The H₂/CO ratio at the highest CH₄ conversion is below 1 because desorbed CO₂ reacts with H2 produced from DRM to produce CO via rWGS, $CO_2(g) + H_2(g) \leftrightarrow CO(g) + H_2O(g)$. In addition to the DRM reaction, CH_4 decomposed to coke and H_2 , $CH_4(g) \leftrightarrow C(s) +$ 2H₂(g), after complete CO₂ desorption. For Ca₂Ni_{0.02}Ti_{0.98} and Ca₂Ni_{0.05}Ti_{0.95} MFMs, the deposited coke was in-situ gasified by lattice oxygen in CaTiO₃.

At the 2nd CO₂ capture step, in addition to the Ni species oxidation, coke deposited during the 1st DRM step was gasified by CO₂ to CO via reverse Boudouard reaction at the beginning of the reaction, $C(s) + CO_2(g) \leftrightarrow 2CO(g)$. Therefore, the CO produced at the 2nd CO2 capture is significantly higher than at the 1st cycle. At the 2nd DRM step, Ca₂Ni_{0.05} DFM exhibited similar results to the first DRM step. For the Ca₂Ni_{0.02}Ti_{0.98} MFM, a small amount of CO gas was produced at the beginning of the reaction (48-50 min). This phenomenon is assumed that $Ca_{1+x}Ni_vTi_{1-v}O_3$ was reduced by CH₄ to make CO and H₂, Ca_{1+x}Ni_yTi_{1-y}O_{3- δ}(s)

+ $\beta \text{CH}_4(g) \leftrightarrow \alpha \text{Ni}^0/\text{Ca}_{1+x-\alpha} \text{Ni}_{v-\alpha} \text{Ti}_{1-v} \text{O}_{3-\delta'}(s) + \beta \text{CO}(g) + 2\beta \text{H}_2(g)$. Then the produced H₂ reacts subsequently with desorbed CO₂ to CO via rWGS, $CO_2(g) + H_2(g) \leftrightarrow CO(g) + H_2O(g)$. This implies that the partially re-incorporated Ni nanoparticles during the rapid CO₂ capture step were easily reduced under the CH₄ stream compared to the 1st cycles. Ca2Ni0.05 Ti0.95 MFM exhibited a notable increase in CO and H2 production at the beginning of the reaction (46 - 50 min). In the XRD results after the DRM step, all CaCO₃ converted to CaO and small Ni⁰ peak appeared after 30 cycles of ICCDRM (Figure S20c,d, Supporting Information).

Figure 11 exhibited CO₂ capture capacity, syngas (CO and H₂) productivity, and H₂/CO ratio of Ca₂Ni_{0.05}, Ca₂Ni_{0.02}Ti_{0.98}, and Ca₂Ni_{0.05}Ti_{0.95} during 30 cycles of ICCDRM at 700 °C to compare the CO₂ capture efficiency, catalytic activity, and deactivation properties during cyclic tests. CO₂ capture capacity and syngas productivity were calculated from the CO₂ breakthrough curves and DRM profiles, respectively. H₂/CO ratio is calculated from the overall CO and H₂ productivity during the DRM step. At the 1st cycle, CO₂ capture capacity of Ca₂Ni_{0.05}, Ca₂Ni_{0.02}Ti_{0.98}, and $Ca_2Ni_{0.05}Ti_{0.95}$ were 8.28, 5.19 and 6.49 mmol CO_2/g ,

www.small-journal.com

16136829, 2024, 36, Downloaded from https://onlinelibrary.wiley.com/doi/1.01002/sml1.202401156 by University of Southern California, Wiley Online Library on [05/02/2025]. See the Terms and Conditions (https://onlinelibrary.wiley.com/rems-and-conditions) on Wiley Online Library for rules of use; OA articles are governed by the applicable Creative Commons.

respectively. Ca₂Ni_{0.05} DFM showed the highest CO₂ capture capacity because of its higher CaO content without CaTiO₃, compared to the Ca₂Ni_{0.02}Ti_{0.98} and Ca₂Ni_{0.05}Ti_{0.95} MFMs. CO₂ capture capacity of Ca₂Ni_{0.05} DFM increased to 10.3 mmol CO₂/g due to the morphology change of CaO/CaCO₃ molecules during the 1st cycle of ICCDRM. Then, it decreased gradually to 7.19 mmol CO₂/g because of the thermal sintering of CaO. The crystallite size of CaO increased from 28.5 to 47.9 nm after 30 cycles of ICCDRM at 700 °C (Table S4, Supporting Information). On the other hand, Ca2Ni0.02Ti0.98 and Ca2Ni0.05Ti0.95 MFMs exhibited stable CO2 capture capacity during the 30 cycles of ICCDRM at 700 °C. This is because the CaTiO₃ acted as a physical barrier intra-region of CaO/CaCO3 molecules, which alleviated the thermal sintering of CaO. The crystallite size of CaO in $Ca_2Ni_{0.02}Ti_{0.98}$ and $Ca_2Ni_{0.05}Ti_{0.95}$ MFM increased slightly after 30 cycles of ICCDRM at 700 °C (Ca₂Ni_{0.02}Ti_{0.98}: 28.1 to 29.9 nm and Ca₂Ni_{0.05}Ti_{0.95}: 24.7 to 31.2 nm).

During the subsequent DRM, syngas productivity of Ca₂Ni_{0.05} DFM increased slightly during the 30 cycles (CO: 3.26 -3.61 mmol CO/g and H_2 : 2.41 – 2.65 mmol H_2 /g) because of higher CO2 capture capacity than that at the 1st cycle. However, the overall H₂/CO ratio decreased slightly from 0.87 to 0.73, resulting from decreased CH₄ decomposition because of severe coke accumulation with cycles. After 30 cycles of ICCDRM, severe Ni nanoparticle sintering and filamentous coke deposition between Ni and large-size nanoparticles were observed in STEM-EDS images (Figure S21, Supporting Information). Cokeencapsulating Ni nanoparticles were not observed in the HRTEM image. For Ca2Ni002Ti098 MFM, syngas (CO and H2) productivity increased slightly, and the H₂/CO ratio was maintained from 0.96 to 1.12. After 30 cycles of ICCDRM at 700 °C, the crystallite size of Ni measured by STEM-EDS images is comparable to that of the freshly reduced samples (Figure S22, Supporting Information). A very thin layer of coke encapsulating Ni nanoparticles was observed in the HRTEM image. For Ca₂Ni_{0.05}Ti_{0.95} MFM, CO productivity at the 1st cycle is 3.74 mmol CO/g and increased to 7.49 mmol CO/g at the 5th cycle because of the increase in CO production at the beginning of the DRM step, as mentioned above. CO productivity decreased gradually to 5.58 mmol CO/g after the 5th cycle. H₂ productivity gradually reduced from 7.56 to 5.37 mmol H_2/g during the 30 cycles. As mentioned above, the H_2/CO ratio at the 1st cycle is 2.02 and then reduced to 0.88 - 1.03because of a significant increase in CO production. Ni nanoparticle sintering was not observed in the STEM-EDS images after 30 cycles of ICCDRM (Figure S23, Supporting Information). In the HRTEM image of $Ca_2Ni_{0.05}Ti_{0.95}$ MFM after 30 cycles of IC-CDRM, coke encapsulating Ni nanoparticles were observed on the Ni with small crystallite size (≈8 nm) that is strongly adhered to the CaTiO₃ perovskite (Figure S23c, Supporting Information). Figure S23d (Supporting Information) shows Ni encapsulated by a thick layer of coke with larger crystallites (≈20 nm) and filamentous coke between Ni and CaTiO₃.

To prove the self-regeneration properties (Ni exsolution and reincorporation) of Ni-doped CaTiO₃/CaO MFM, XPS spectra measurements were conducted after ICCDRM reactions (Figure S24, Supporting Information). Although Ni XPS spectra were unclear due to the low Ni amount in the sample, it was observed that Ni⁰ peak appeared after reduction decreased after carbonation step, and then Ni⁰ peak appeared again after the 1st and 30th DRM steps. During the self-regeneration, not all Ni species were exsolved and some parts of Ni species existed as Ni⁴⁺/Ni³⁺ in the Ca_{1+v}Ni_vTi_{1-v}O₃ perovskite. In the Ca 2p spectra, CaO-to-CaTiO₃ ratio increased after reduction due to the exsolution of CaO, and then decreased after carbonation step, which was accompanied by Ni re-incorporation. After DRM step, CaO-to-CaTiO₃ ratio decreased. In the Ti 2p spectra, binding energy values of Ca2Ni0.02Ti0.98 MFM were lower than those of CaTiO3, as mentioned above (Figure 4). After reduction, Ti 2p peaks shifted to higher biding energy, which is comparable to that of CaTiO₃. The Ti 2p peaks decreased after carbonation, and then increased after DRM step. In the O 1s spectra, a new peak was observed at ≈533 eV after carbonation step, which might be absorbed CO₂ by CaO (CO₃²⁻). However, the peak at \approx 533 eV was still observed after DRM steps. Considering complete conversion of CaCO₃ to CaO in the XRD result, the peak might be attributed to active CHx during DRM step.^[29] Based on the XRD, XPS and STEM results, it is concluded that the exsolved Ni nanoparticles from the Ca_{1+x}Ni_xTi_{1-y}O₃ can be re-incorporated after carbonation (oxidative condition), and then exsolved after DRM step (reductive condition).

Conventional carbonation and decarbonation studies (carbonation: 10 vol% CO₂/He at 700 °C for 15 min and decarbonation: 100 vol% He at 900 °C for 15 min) were conducted over Ca₂Ni_{0.05} DFM and Ca₂Ni_{0.05}Ti_{0.95} MFM to study NiO sintering caused by the stress-induced sintering of CaO/CaCO₃ (Figure S25, Supporting Information). As mentioned above, NiO of Ca2Ni005 DFM and Ca2Ni0.05Ti0.95 MFM are supported on the CaO and the $CaTiO_3$, respectively. The test over $Ca_2Ni_{0.02}Ti_{0.98}$ MFM was not conducted because Ni species exist as $Ca_{1+x}Ni_vTi_{1-v}O_3$ phase without NiO phase in the as-prepared sample. CO₂ capture capacity of $Ca_2Ni_{0.05}$ DFM and $Ca_2Ni_{0.05}Ti_{0.95}$ MFM at the 1st cycle is 16.97 and 6.82 mmol CO_2/g , respectively, because $Ca_2Ni_{0.05}$ DFM contains more CaO contents than that of Ca2Ni005Ti005 MFM. The CO₂ capture capacity of Ca₂Ni_{0.05} DFM decreased gradually to 7.13 mmol CO₂/g at the 15th carbonation due to the morphological changes of the CaO/CaCO3 after decarbonation. For $Ca_2Ni_{0.05}Ti_{0.95}$ MFM, CO_2 capture capacity slightly reduced from 6.82 to 4.56 mmol CO₂/g during 15 cycles of carbonation and decarbonation. The deactivation rate of CO₂ capture capacity during 15 cycles over $Ca_2Ni_{0.05}$ DFM was \approx 5.4-fold faster than that over Ca₂Ni_{0.05}Ti_{0.95} MFM because CaTiO₃ addition between CaO grains suppressed the agglomeration from the volume expansion of CaO/CaCO₃ during CO₂ capture in Ca₂Ni_{0.05}Ti_{0.95} MFM. The crystallite size of NiO and CaO before and after 15 cycles of carbonation/decarbonation were calculated using the Scherrer equation and are summarized in Table \$5 (Supporting Information). The crystallite size of CaO in Ca₂Ni_{0.05} DFM increased from 28.5 to 34.0 nm. The changes in surface morphology and porosity of Ca₂Ni_{0.05} DFM from volume expansion of CaO/CaCO₃ structures, as well as relatively weak NiO-CaO interaction, could result in the aggregation of Ni species (15.9 to 38.2 nm) during the carbonation and decarbonation cycles. In contrast, the crystallite sizes of CaO and NiO of $Ca_2Ni_{0.05}Ti_{0.95}$ MFM are comparable before and after 15 cycles of carbonation/decarbonation (CaO: 24.3 to 26.0 nm, and NiO: 14.0 to 12.7 nm). The presence of CaTiO₂ in the intra-region of CaO grains could suppress the severe aggregation of CaO during carbonation and decarbonation cycles. In addition, NiO supported on CaTiO₃ instead

16136829, 2024, 36, Downloaded from https://onlinelibrary.wiley.com/doi/10.1002/sml1202401156 by Universiy Of Southern California, Wiley Online Library on [05/02/2025]. See the Terms and Conditions (https://onlinelibrary.wiley.com/term

and-conditions) on Wiley Online Library for rules of use; OA articles are governed by the applicable Creative Commons

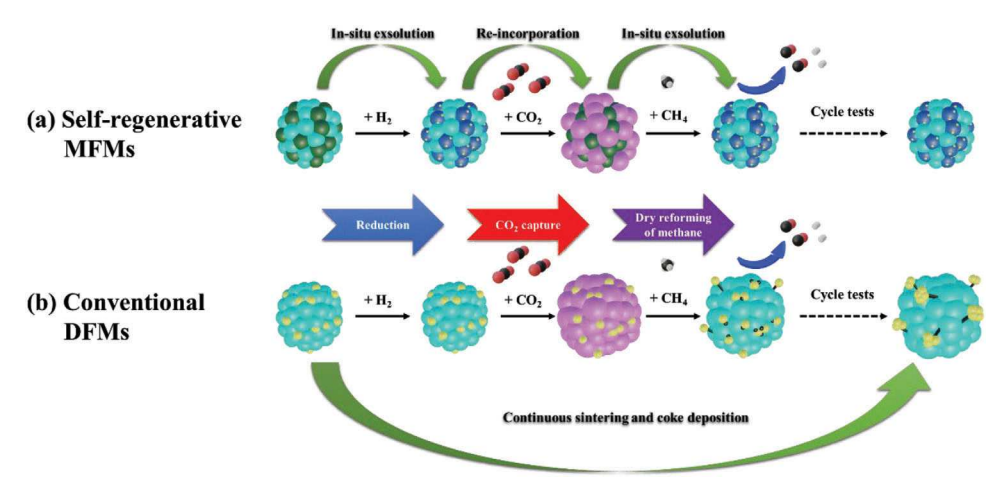


Figure 12. Schematics of ICCDRM over a) self-regenerative Ni-doped CaTiO₃/CaO and b) conventional Ni/CaO DFM; dark green (Ca_{1+a}, Ni_xTi_{1-x}O₃), cyan (CaO), blue (CaTiO₃), yellow (Ni), purple (CaCO₃), black (coke).

of CaO/CaCO3 decreases the occurrence of NiO mobility and sintering.

2.4. Mechanism of ICCDRM Over Self-Regenerative Ni-Doped CaTiO₃/CaO MFM

Based on the physicochemical analysis and experimental results, a schematic of the mechanism over the self-regenerative Ni-doped CaTiO₃/CaO (Ca₂Ni_{0.02}Ti_{0.98}) MFM and conventional Ni/CaO (Ca2Ni005) DFM in the ICCDRM process was illustrated (Figure 12). For conventional Ni/CaO DFM, NiO supported on CaO is reduced to Ni metal under the H2 reduction step, $xNiO/CaO(s) + xH_2(g) \leftrightarrow xNi^0/CaO(s) + xH_2O(g)$. During the CO₂ capture step, the metallic Ni is oxidized by CO₂ (oxidative condition) to produce CO, and CaO captures CO₂ to produce $CaCO_3$, $xNi^0/CaO(s) + (x+1)CO_2(g) \leftrightarrow xNiO/CaCO_3(s) + xCO(g)$. During the DRM step, NiO is reduced under CH₄ (reductive condition), and CO2 desorbs from CaCO3 and reacts with CH4 to produce syngas (CO and H₂). In addition to DRM, CH₄ is decomposed to coke and H₂, exacerbating the formation of filamentous coke growth between Ni and CaO. The overall reaction is as follows: $xNiO/CaCO_3(s) + (x+y+1)CH_4(g) \leftrightarrow yC-xNi^0/CaO(s)$ + $(x+2)CO(g) + 2(x+y+1)H_2(g)$. The stress induced by the cyclical volume expansion and shrinkage from CaO to CaCO₃ (CaO: 16.9 cm³/g and CaCO₃: 36.9 cm³ g⁻¹) during carbonation and decarbonation^[9] can contribute to rapid pore collapse of the structure. Additionally, the lower Tammann temperature of CaCO₃ (533 °C) than the DRM operation temperature (\approx 700 °C) causes the loss of surface area, porosity, and sintering-induced decrease in CO₂ capture capacity. [9,10] During each cycle, the reversible phase transformation of CaO to CaCO3 weakens the Ni-CaO metal support interaction, resulting in significant sintering of Ni nanoparticles on the surface of CaO.[11]

For the self-regenerative Ni-doped CaTiO3/CaO MFM, Ni nanoparticles are assembled and formed via exsolution from the $Ca_2Ni_{0.02}Ti_{0.98}$ perovskite lattice. The formed Ni nanoparticles are evenly distributed and partially submerged or socketed in the CaTiO₃ perovskite oxide support and can be described by the equation: $Ca_{1+x}Ni_{y}Ti_{1-y}O_{3-\delta}/(1-x)CaO(s) + \beta H_{2}(g)$ $\leftrightarrow \alpha \text{Ni}^0/\text{Ca}_{1+x-\alpha} \text{Ni}_{y-\alpha} \text{Ti}_{1-y} \text{O}_{3-\delta'}/(1-x) \text{CaO(s)} + \beta \text{H}_2 \text{O(g)}. \text{ During}$ the CO2 capture step, exsolved Ni nanoparticles are reincorporated into the subsurface of the CaTiO₃ lattice (e.g., self-regeneration) under CO2 (oxidative condition), which is accompanied by CO production, and CaO reacts with CO2 to produce $CaCO_3$; $\alpha Ni^0/Ca_{1+x-\alpha}Ni_{y-\alpha}Ti_{1-y}O_{3-\delta'}/(1-x)CaO(s) + (\beta+1-x)CaO(s)$ $x)CO_2(g) \leftrightarrow Ca_{1+x}Ni_vTi_{1-v}O_{3-\delta}/(1-x)CaCO_3(s) + \beta CO(g)$. Ni-doped CaTiO₃/CaO MFMs exhibited stable CO₂ capture capacity during cyclic ICCDRM because CaTiO3 acts as a physical barrier between CaO grains, suppressing the CaO sintering from CaO/CaCO₃ volume expansion. During the subsequent DRM step, Ni nanoparticles exsolved from Ca2Ni0.02 Ti0.98 perovskite under CH4 (reductive condition) and CO2 desorbed from CaCO3 reacts with CH4 to produce syngas (CO and H_2), $Ca_{1+x}Ni_vTi_{1-v}O_{3-\delta}/(1-x)CaCO_3(s) + (\beta+1-x)CH_4(g) \leftrightarrow$ $\alpha \text{Ni}^{0}/\text{Ca}_{1+x-\alpha} \text{Ni}_{y-\alpha} \text{Ti}_{1-y} \text{O}_{3-\delta'}/(1-x) \text{CaO(s)} + (\beta+2-2x) \text{CO(g)} + 2(\beta+1-x) \text{CaO(s)}$ x)H₂(g). Moreover, Tammann temperatures of Ni and NiO are much higher (Ni: 863 °C and NiO: 1114 °C) than the typical DRM operation temperature (700 °C).[10] This means the Ni sintering in the Ca₂Ni_{0.05} DFM is predominately caused by the volume expansion (CaO to CaCO₃) and weak interaction between Ni and CaO during the cyclic ICCDRM. Therefore, the separation of Ni species socketed in CaTiO₃ from CaO grains prevents significant Ni sintering and prolongs ICCDRM activity.

3. Conclusions

In this paper, Ni-doped CaTiO₃/CaO nanocomposite (Ca2Ni0.02Ti0.98) as MFMs was prepared for ICCDRM. A small amount of Ni can be incorporated into CaTiO₃ perovskite as a $Ca_{1+x}Ni_vTi_{1-v}O_3$ perovskite because of an unstable NiO₆ octahedron. In-situ exsolved Ni nanoparticles, which interact strongly with the CaTiO₃ perovskite oxide support, were evenly distributed on the surface after reductive conditions (H2 or CH₄). The Ni nanoparticles exsolved in CaTiO₃ migrate back to the subsurface during CO2 capture (oxidative conditions), resulting in self-regeneration. In addition, in-situ exsolved Ni nanoparticles, which interact strongly with host CaTiO₃

SMQII

16136829, 2024, 36, Downloaded from https://onlinetibrary.wiley.com/doi/10.1002/smll.202401156 by University Of Southern California, Wiley Online Library on [05/02/2025]. See the Terms and Conditions (https://onlinetibrary.wiley.com/terms/

and-conditions) on Wiley Online Library for rules of use; OA articles are governed by the applicable Creative Commons

perovskite, exhibited excellent resistance to filamentous coke deposition under CH4 conditions. Some deposited coke was in situ gasified by surface lattice oxygen of CaTiO₃ perovskite. The Ni-doped CaTiO₃/CaO MFM showed relatively stable CO₂ capture capacity and syngas productivity during 30 cycles of IC-CDRM. The presence of CaTiO₃ between CaO grains prevented volume expansion, maintaining the CO₂ capture capacity. The strong interaction between Ni and CaTiO3, separation from CaO/CaCO3 morphology change, and self-regeneration during CO2 capture and subsequent DRM (redox condition) can mitigate Ni sintering. Due to the small size of exsolved Ni particles and their strong interaction with CaTiO3, there was no severe coke build-up. Additionally, coke gasification occurred by lattice oxygen during the CO₂ capture process. Therefore, our results show that Ni-doped CaTiO₃/CaO MFM can potentially overcome current challenges for the ICCDRM process. Future efforts will optimize the self-regenerative MFMs for improved ICCDRM performance and multicycle stability.

4. Experimental Section

Preparation of MFMs: The $Ca_xNi_yTi_{1-y}$ (x=1, and 2, and y=0, 0.01, 0.02, and 0.05) perovskite materials were prepared using the sol-gel Pechini method. $Ni(NO_3)_2 \cdot 6H_2O$ (Alfa Aesar), $Ca(NO_3) \cdot 4H_2O$ (Sigma–Aldrich), and $Ti(C_4H_9O)_4$ (Arcros Organics) were used for the Ni, Ca and Ca in precursors, respectively. Citric acid (Alfa Aesar) and ethylene glycol butyl ether (Sigma–Aldrich) were used as chelating and polymerization agents. The required amounts of metal precursors were mixed in a stoichiometric ratio and dissolved in DI water to form an aqueous solution. Citric acid (the molar ratio of citric acid to metal ions was 1) and ethylene glycol butyl ether (the molar ratio of citric acid to ethylene glycol butyl ether was 3) were added into the precursor solution. The solution was dried in an oven overnight at 120 °C to form a dried gel. The resulting gel was ground finely with mortar and pestle and calcined in a muffle furnace at 800 °C for 5 h with a temperature ramp rate of 5 °C min⁻¹.

using a Cu K α radiation source. The crystallite sizes of CaO and NiO were calculated using the Scherrer equation. The chemical composition of the surface of MFMs was obtained in an XPS using an Axis Ultra spectrometer (Kratos Analytical) equipped with an Al K α source. The atomic resolution images and crystalline phase of the MFMs were obtained by STEM-HAADF and HRTEM using a ThermoFischer Scientific Titan Themis 300 with double spherical aberration-correctors operated at 300 kV. TPR was used to investigate the reducibility of the MFMs (50 mg) under 5% H₂/He (H₂-TPR) or 10% CH₄/He (CH₄-TPR) with total flow rate of 50 ml min⁻¹ from 100 to 800 °C with temperature ramping of 10 °C min⁻¹ after pretreatment in 20% O₂/He condition at 800 °C for 1 h in a quartz tube microreactor (Hiden Analytical CATLAB) combined with a MS spectrometer (Hiden QGA Gas Analyzer). TPO was conducted under 20 vol% ${\rm O_2/He}$ from 100 to 800 $^{\circ}{\rm C}$ with a temperature ramping rate of 10 °C min⁻¹ in a quartz tube microreactor (Hiden Analytical CATLAB) and MS spectrometer (Hiden QGA Gas Analyzer) to determine the type of coke species after CH₄-treatment under 10 vol% CH_4 /He with total flow rate of 50 ml min⁻¹ at 800 °C for 1 h over

Reaction Process: The CO_2 capture and subsequent DRM was conducted using 50 mg of MFMs in a quartz tube microreactor (Hiden Analytical CATLAB) combined with an MS spectrometer (Hiden QGA Gas Analyzer) after reduction under 5% H_2/He condition at 800 °C for 1 h. The temperature was decreased to 600, 650, and 700 °C, which was maintained during the reaction. At the CO_2 capture step, 10 vol% CO_2/He flowed through the bed with 50 ml min $^{-1}$ total flow rate for 15 min. At the subsequent DRM step, the gas composition changed to 10 vol% CH_4 and was maintained for 15 min.

Conventional carbonation and decarbonation was carried out using 50 mg of MFMs in a quartz tube microreactor (Hiden Analytical CATLAB) combined with an MS spectrometer (Hiden QGA Gas Analyzer) after pretreatment in 20% O $_2$ /He condition at 800 °C for 1 h. At the CO $_2$ capture step, 10 vol% CO $_2$ /He flowed through the bed with 50 ml min $^{-1}$ of total flow rate at 700 °C for 15 min. At the regeneration step, the temperature increased to 900 °C with temperature ramping of 10 °C min $^{-1}$ and maintained under pure He for 15 min.

 ${\rm CO_2}$ capture capacity during ${\rm CO_2}$ capture step, syngas (CO and ${\rm H_2}$) productivity during DRM step and ${\rm H_2/CO}$ ratio were calculated following equations (3)–(5):

$$CO_{2} \text{ capture capacity (mmol/g) during } CO_{2} \text{ capture} = \frac{\int \left\{ \text{Inlet } CO_{2} \text{ molar flow rate } \left(\frac{mmol}{min} \right) - \text{Outlet } CO_{2} \text{ molar flow rate } \left(\frac{mmol}{min} \right) \right\} dt}{\text{Weight of sample (g)}}$$
(3)

Syngas (CO and H₂) productivity (mmol/g) during DRM =
$$\frac{\int Produced syngas (CO or H2) molar flow rate $\left(\frac{mmol}{min}\right) dt}{Weight of sample (g)}$ (4)$$

Perovskite Structure Factors: The perovskite structure factors were calculated to predict the stability of the perovskite oxide structure. The Goldschmidt tolerance factor, t, of perovskite (ABO₃), is defined as follows:

$$t = \frac{r_A + r_O}{\sqrt{2} (r_B + r_O)} \tag{1}$$

Octahedron factor, $\mu_{\text{\tiny I}}$ related to octahedral unit BO $_{\text{\tiny 6}}$, is defined as follows:

$$\mu = \frac{r_B}{r_O} \tag{2}$$

where r_A and r_B are the ionic radius of the A and B cations, respectively, and r_O is the ionic radius of the O anion.

Materials Characterization: The crystallographic structure of the MFMs was characterized by XRD analysis (PANalytical Empyrean Series 2)

 $H_2/COratio = H_2 productivity/COproductivity$ (5)

Supporting Information

Supporting Information is available from the Wiley Online Library or from the author.

Acknowledgements

This research was supported by the National Science Foundation (CBET: No. 2143578).

Conflict of Interest

The authors declare no conflict of interest.

www.advancedsciencenews.com

www.small-journal.com

Data Availability Statement

The data that support the findings of this study are available from the corresponding author upon reasonable request.

Keywords

dry reforming of methane, integrated CO₂ capture and utilization, multifunctional materials, nickel doped-calcium titanates, self-regeneration

> Received: February 13, 2024 Revised: March 27, 2024 Published online: April 30, 2024

- [1] a) E. García-Bordejé, A. B. Dongil, J. Moral, J. M. Conesa, A. Guerrero-Ruiz, I. Rodríguez-Ramos, J. CO2 Util. 2023, 68, 102370; b) C. Jeong-Potter, A. Porta, R. Matarrese, C. G. Visconti, L. Lietti, R. Farrauto, Appl. Catal., B 2022, 310, 121294; c) S. Jo, J. H. Lee, T. Y. Kim, J. H. Woo, H.-J. Ryu, B. Hwang, S. C. Lee, J. C. Kim, K. L. Gilliard-AbdulAziz, Fuel 2022, 311, 122602; d) S. Jo, H. D. Son, T.-Y. Kim, J. H. Woo, J. C. Kim, S. C. Lee, K. L. Gilliard-AbdulAziz, Chem. Eng. J. 2023, 143772; e) S. J. Park, M. P. Bukhovko, C. W. Jones, Chem. Eng. J. 2021, 420, 130369; f) J.-H. Woo, S. Jo, J.-E. Kim, T.-Y. Kim, H.-D. Son, H.-J. Ryu, B. Hwang, J.-C. Kim, S.-C. Lee, K. L. Gilliard-AbdulAziz, Catalysts 2023, 13, 1174.
- [2] S. Jo, L. Cruz, S. Shah, S. Wasantwisut, A. Phan, K. L. Gilliard-AbdulAziz, ACS Catal. 2022, 12, 7486.
- [3] S. B. Jo, J. H. Woo, J. H. Lee, T. Y. Kim, H. I. Kang, S. C. Lee, J. C. Kim, Sustainable Energy Fuels 2020, 4, 4679.
- [4] a) J. Hu, P. Hongmanorom, V. V. Galvita, Z. Li, S. Kawi, Appl. Catal., B 2021, 284, 119734; b) S. Jo, J. H. Lee, J. H. Woo, T.-Y. Kim, H.-J. Ryu, B. Hwang, J. C. Kim, S. C. Lee, K. L. Gilliard-AbdulAziz, Sustainable Energy Fuels 2022, 6, 81; c) S. B. Jo, J. H. Woo, J. H. Lee, T. Y. Kim, H. I. Kang, S. C. Lee, J. C. Kim, Sustainable Energy Fuels 2020, 4, 5543; d) H. Sun, J. Wang, J. Zhao, B. Shen, J. Shi, J. Huang, C. Wu, Appl. Catal., B 2019, 244, 63; e) S. Tian, F. Yan, Z. Zhang, J. Jiang, Sci. Adv. 2019, 5, eaav5077; f) B. Shao, Z.-Q. Wang, X.-Q. Gong, H. Liu, F. Qian, P. Hu, J. Hu, Nat. Commun. 2023, 14, 996.
- [5] S. Lawson, K. Baamran, K. Newport, F. Rezaei, A. A. Rownaghi, *Chem. Eng. J.* 2022, 431, 133224.
- [6] Y. Chai, Y. Fu, H. Feng, W. Kong, C. Yuan, B. Pan, J. Zhang, Y. Sun, ChemCatChem 2018, 10, 2078.
- [7] a) B. Bao, J. Liu, H. Xu, B. Liu, W. Zhang, RSC Adv. 2016, 6, 68934; b)
 A. Ochoa, J. Bilbao, A. G. Gayubo, P. Castaño, Renewable Sustainable Energy Rev. 2020, 119, 109600.
- [8] A. Ochoa, B. Valle, D. E. Resasco, J. Bilbao, A. G. Gayubo, P. Castaño, ChemCatChem 2018, 10, 2311.
- [9] H. J. Yoon, K. B. Lee, Chem. Eng. J. 2019, 355, 850.
- [10] M. D. Argyle, C. H. Bartholomew, Catalysts 2015, 5, 145.

- [11] Z. Lv, C. Qin, S. Chen, D. P. Hanak, C. Wu, Sep. Purif. Technol. 2021, 277, 119476.
- [12] a) P. Cao, P. Tang, M. F. Bekheet, H. Du, L. Yang, L. Haug, A. Gili, B. Bischoff, A. Gurlo, M. Kunz, J. Phys. Chem. C 2021, 126, 786; b) S. Shah, J. Hong, L. Cruz, S. Wasantwisut, S. R. Bare, K. L. Gilliard-AbdulAziz, ACS Catal. 2023, 13, 3990; c) S. Shah, S. Sayono, J. Ynzunza, R. Pan, M. Xu, X. Pan, K. L. Gilliard-AbdulAziz, AIChE J. 2020, 66, e17078; d) S. Shah, M. Xu, X. Pan, K. L. Gilliard-Abdulaziz, ACS Appl. Nano Mater. 2021, 4, 8626; e) S. Shah, M. Xu, X. Pan, K. L. Gilliard-AbdulAziz, ACS Appl. Nano Mater. 2022, 5, 17476; f) J. Zhang, M.-R. Gao, J.-L. Luo, Chem. Mater. 2020, 32, 5424; g) M. Najimu, S. Jo, K. L. Gilliard-AbdulAziz, Acc. Chem. Res. 2023, 3990.
- [13] Q. Ji, L. Bi, J. Zhang, H. Cao, X. S. Zhao, Energy Environ. Sci. 2020, 13, 1408
- [14] J. H. Kim, J. K. Kim, J. Liu, A. Curcio, J.-S. Jang, I.-D. Kim, F. Ciucci, W. Jung, ACS Nano 2020, 15, 81.
- [15] R. Huang, C. Lim, M. G. Jang, J. Y. Hwang, J. W. Han, J. Catal. 2021, 400, 148.
- [16] A. Umar, M. O. Thotyl, GCB Bioenergy 2023, 15, 791.
- [17] a) C. Lin, A. C. Foucher, Y. Ji, C. D. Curran, E. A. Stach, S. McIntosh, R. J. Gorte, ACS Catal. 2019, 9, 7318; b) C. Lin, J. B. Jang, L. Zhang, E. A. Stach, R. J. Gorte, ACS Catal. 2018, 8, 7679.
- [18] a) M. Heidari, M. Tahmasebpoor, S. B. Mousavi, C. Pevida, J. CO2 Util. 2021, 53, 101747; b) C. Zhang, Y. Li, Z. He, J. Zhao, D. Wang, Appl. Catal., B 2022, 314, 121474.
- [19] a) A. Ali, A. Zaman, M. K. Khan, L. B. Farhat, A. H. Jabbar, K. M. Badi,
 I. Ullah, V. Tirth, S. Khan, J. Supercond. Novel Magn. 2022, 35, 1987. b)
 H. Wu, W. Cai, C. Zhou, R. Yang, R. Gao, G. Chen, X. Deng, Z. Wang,
 X. Lei, C. Fu, J. Mater. Sci.: Mater. Electron. 2021, 32, 24328.
- [20] Y. Li, R. Zhu, Y. Wang, L. Feng, Y. Liu, npj Computat. Mater. 2023, 9, 109
- [21] a) D. Ji, C. Liu, Y. Yao, L. Luo, W. Wang, Z. Chen, Nanoscale 2021, 13, 9952; b) T. L. Phan, N. Tran, D. H. Kim, P. T. Tho, B. T. Huy, T. N. Dang, D. S. Yang, B. Lee, J. Am. Ceram. Soc. 2018, 101, 2181.
- [22] S. AlZadjali, Z. Matouk, A. AlShehhi, N. Rajput, M. Mohammedture, M. Guttierrez, Appl. Sci. 2023, 13, 1707.
- [23] a) Z. Fu, J. Hu, W. Hu, S. Yang, Y. Luo, Appl. Surf. Sci. 2018, 441, 1048;
 b) Y. Shi, L. Wang, M. Wu, F. Wang, Appl. Catal., B 2023, 337, 122927.
- [24] J. Hu, P. Hongmanorom, P. Chirawatkul, S. Kawi, Chem. Eng. J. 2021, 426, 130864.
- [25] Y. Qiu, R. Gao, W. Yang, L. Huang, Q. Mao, J. Yang, L. Sun, Z. Hu, X. Liu, Chem. Mater. 2020, 32, 1864.
- [26] H. Guo, S. Wang, C. Li, Y. Zhao, Q. Sun, X. Ma, Ind. Eng. Chem. Res. 2016, 55, 7873.
- [27] J. Zhao, X. Cao, Y. Bai, J. Chen, C. Zhang, Optical Mater. 2023, 135, 113239.
- [28] a) H. Idriss, Surf. Sci. 2021, 712, 121894; b) J. Liu, M. Liu, S. Chen, B. Wang, J. Chen, D.-P. Yang, S. Zhang, W. Du, Green Energy Environ. 2022, 7, 352.
- [29] A. Salcedo, P. G. Lustemberg, N. Rui, R. M. Palomino, Z. Liu, S. Nemsak, S. D. Senanayake, J. A. Rodriguez, M. V. Ganduglia-Pirovano, B. Irigoyen, ACS Catal. 2021, 11, 8327.